Spontaneous Formation of Magnetic Moments and Dephasing in Two-Dimensional Disordered Systems

Thesis submitted in partial fulfillment of the requirements for the degree of

"DOCTOR OF PHILOSOPHY"

by

Roi Levy

Submitted to the Senate of Ben-Gurion University of the Negev

April 2, 2013

Beer-Sheva

Spontaneous Formation of Magnetic Moments and Dephasing in Two-Dimensional Disordered Systems

Thesis submitted in partial fulfillment of the requirements for the degree of

"DOCTOR OF PHILOSOPHY"

by

Roi Levy

Submitted to the Senate of Ben-Gurion University of the Negev

Approved by the advisor

Approved by the Dean of the Kreitman School of Advanced Graduate Studies

April 2, 2013

Beer-Sheva

This work was carried out under the supervision of

Prof. Yigal Meir

In the Department of Physics

Faculty of Natural Sciences

Abstract

Quantum point contacts (QPCs) are the ultimate building blocks for controlling nanoscale electron transport. However, various observations highlight the importance of electron many-body effects, not well understood, in the physics of QPCs. An example is the hotly debated 0.7 anomaly in the quantized conductance trace. A novel experiment by C. H. van der Wal group in Groningen reports a setup that allows in-situ tuning of the QPC length, revealing signatures of both single- and two-impurity Kondo physics in transport around the 0.7 anomaly, which is in agreement with theory. Both the 0.7 anomaly and the Kondo signatures show a periodic modulation as a function of QPC length, which can be explained by a varying number of spontaneously localized states. We show using spin-density-functional theory calculations that the number of spontaneously localized states increases as the QPC becomes longer due to the larger number of Friedel oscillations enclosed within the QPC. These changes in the parity of the localized states that are consistent with a periodic modulation between single-peak and double-peak. This can explain the experimental results in terms of transport through single and paired Kondo states.

Since QPCs form naturally in the saddle-points of two dimensional disordered systems, we want to see whether such localized states form in two-dimensional disordered system, and how they affect the coherence time. From theory, one expects a power law dependence of the dephasing rate on temperature, which was confirmed in experiments at that temperature range. However, when decreasing the temperature further many experiments shows an apparent saturation in the coherence time. Our numerical SDFT simulation show that Friedel oscillations can develop into self-consistent localized states in an open two-dimensional systems. These states are formed at various saddle points of the disorder potential depending

on the electron bulk density, and can explain apparent saturation of the coherence time observed in experimental studies through spin flip scattering.
Last we studied the effect of dephasing under strong magnetic field where experimental studies showed that the transition from the last quantum Hall plateau in the integer quantum Hall effect terminates with a unique insulating phase. This phase is characterized by the divergence of the longitudinal resistivity with decreasing temperature, while the Hall resistivity remains quantized to its value in the last plateau. This is in contradiction to the predictions of the non-interacting electron theory. Therefore, it was suggested that this quantum Hall Insulator phase may be related to incoherent scattering events. We show that by including rare incoherent scattering events into Chalker-Coddington network, the quantum Hall insulator becomes a stable phase. The theory also predicts a non-monotonic dependence of the Hall resistance on system size.

(The last subject was addressed in my M.Sc. thesis using real space renormalization group. The report here is based on a full numerical solution of the network and includes only work that I did during my Ph.D. studies)

Keywords: Quantum Point contact, 0.7 anomaly, Zero-Bias anomaly, Coherence time, Quantum Hall insulator.

The work in this thesis was published in the following papers:

1) R. Levy and Y. Meir, "Theory of the Quantum Hall Insulator," arXiv:1005.5245v2, 2010.

2) M. J. Iqbal, R. Levy, E. J. Koop, J. B. Dekker, J. P. de Jong, J. H. M. van der Velde, D. Reuter, A. D. Wieck, R. Aguado, Y. Meir, and C. H. van der Wal, Odd and even kondo effects from emergent localization in quantum point contacts, Nature, vol. 501, pp. 7983, 2013.

Contents

Abstract **i**

Introduction **1**

1 Emergent Localized States in Length Tuned Quantum Point Contacts **5**

1.1 Many Body Physics in Quantum Point Contacts 5

1.2 Experimental Results from Length-Tunable QPCs 9

1.3 Spin Density Functional Theory Results 10

1.4 Conclusion 19

2 Dephasing in Two-Dimensional Disordered Systems **20**

2.1 Theoretical Models 21

2.2 Experimental Evidence 23

2.3 Spin Density Functional Theory Results 30

2.4 Conclusions 38

3 Low Temperature Dephasing and the Quantized Hall Insulator **39**

3.1 Integer Quantum Hall Effect 39

3.2 Quantized Hall Insulator 42

3.2.1 Experimental Evidence 43

3.2.2 Theoretical Models 43

3.3 Incoherent Scattering 47

3.4 Model and Results 49

3.5 Conclusion 57

Conclusion **58**

Appendix **59**

A Spin Density Functional Theory **59**

A.1 Hohenberg Kohn Theorems 60

A.2 Kohn-Sham Scheme 62

B Detailed Calculation for a Chalker and Coddington Network with Dephasing **64**

Bibliography **75**

Introduction

This thesis deals with three projects that I carried out in the field of mesoscopic physics. The first deals with quantum point contact (QPC) which is a narrowing of the transport channel in a two-dimensional electron gas(2DEG) heterostructure and is a basic nano-electronic device. When the transport is ballistic, the conductance is quantized to $2e^2/h * N$ [1] where e is the electron charge, h is Planck's constant, and N is the number of transverse modes in the QPC, where the factor of two accounts for spin degeneracy. This can be understood within the non-interacting picture; but, even in the cleanest samples, there are deviations from this quantization due to electron-electron interaction [2, 3]. First, there is an additional small plateau at the linear conductance trace at about $0.7 \cdot (2e^2/h)$ (0.7 anomaly). Second, the nonlinear differential conductance typically shows a peak around zero bias (Zero-Bias Anomaly, ZBA) at conductance levels between quantized plateaus. These two signatures are reminiscent of the Kondo effect seen in quantum dots containing an odd number of electrons [4, 5, 6, 7, 8, 9, 10], and they are quite surprising as QPC is an open system.

In order to address this problem a spin density functional theory (SDFT) calculation of a QPC in a multi-channel wire in a hetro-structure was carried [11], revealing the formation of self-consistent or emergent localized states (ELSs), each having one electron charge inside the QPC. This theoretical work has developed the picture that the many-body effects in QPC channels are intimately related to the occurrence of Friedel oscillations – oscillations in the electron charge density that occur when electron waves are reflected in a partially open QPC

channel, which is enhanced into an ELS with about one electron of charge due to Coulomb repulsion and exchange interactions between electrons. The repulsion of electrons by the ELS (a precursor of the Coulomb blockade) can thus reduce the conductance, thereby explaining the observation of the 0.7 anomaly. In addition, transport through such a state can carry signatures of the Kondo effect [12]. It also predicted that, depending on parameters, a pair of such ELSs may emerge in the channel, resulting in a split peak ZBA, similar to that observed in double quantum dots [13], due to the double-impurity Kondo effect [14, 15, 16, 17].
In a novel experiment a configuration of 6 gates voltage (as as opposed to regular QPC with 2 gates voltage) create a QPC that allows in-situ tuning of the QPC length [18]. This length tunable QPC reveals signatures of both single- and two-impurity Kondo physics in transport around the 0.7 anomaly. Both the 0.7 anomaly and the Kondo signatures show a periodic modulation as a function of QPC length, which can be explained by a varying number of spontaneously localized states. We show using SDFT calculations that the number of spontaneously localized states increases as the QPC becomes longer due to the larger number of Friedel oscillations enclosed within the QPC. The increasing in number of localized states with QPC length is consistent with the periodic modulation between single-peak and double-peak. This can explain the experimental results in terms of transport through single and paired Kondo states.

The second project deals with coherence time - the time over which the phase of the wave function is maintained - is one of the fundamental properties in quantum mechanics, and is especially important for mesoscopic systems where the coherence length is of the order of the sample size. From basic quantum mechanical arguments, one expects that as the temperature goes down the external degrees of freedom freeze out, so that coherence time will be infinite at zero temperature. For temperatures less than one Kelvin, the phonon's contribution to dephasing becomes negligible and the main processes of dephasing are due to electron-electron interactions. The theory [19, 20] predict a power law dependence of the

dephasing rate on temperature, which was confirmed in experiments. However, when the temperature is decreased further, there is apparent saturation in the coherence time [21, 22, 23, 24, 25, 26, 27, 28, 29] which is in contradiction with the electron-electron interaction picture, and possibly with the general quantum mechanical principle described above. One possible explanation for this saturation is magnetic impurities: At temperatures higher than the Kondo temperature, there is a finite probability for spin flip scattering that will cause dephasing. Follow-up experiments [28] have demonstrated that a small amount of magnetic impurities changes the temperature dependence of the phase coherence time τ_ϕ from a power law to saturation at low temperatures as depicted in figure 2.2. However, the conductors of the original experiments [26] claim that they checked and found that no magnetic impurities exist in their system. Moreover, one does not expect any magnetic impurities in semiconductor systems, where the saturation in coherence time has also been seen [22, 23, 24, 27]. Since QPCs form naturally at the saddle-points of a two-dimensional disordered systems, one can ask: Can these magnetic moments be formed in a two dimensional disordered systems? And, if so, are they responsible for the saturation of the coherence time?
To address this question we extended our numerical SDFT simulation to an open two-dimensional system with disorder potential, and show that Friedel oscillations can develop into self-consistent localized states. These states are formed at various saddle points of the disorder potential depending on the electron bulk density, and can explain apparent saturation of the coherence time observed in experimental studies through spin flip scattering.

The last subject of the thesis considers the effect of dephasing under a strong magnetic field. We deal with this problem in the semiclassical regime using the Chalker-Coddington (CC) [30] scattering network with the addition of current conserving reservoirs [31] in front of each scatterer. These current conserving reservoirs act as sources of dephasing – for every electron that enters a reservoir, there is an electron that leaves it. However, the phase of the outgoing electron has no correlation with the phase of the incoming electron, so that

interference effects are impeded . The probability of the electron to enter the reservoir is controlled by adding a scatterer in front of the reservoir, which allow us to control the dephasing rate in the system.

One use for this kind of network is to study the quantum Hall insulator phase. Experimental studies showed that the transition from the last quantum Hall plateau in the integer quantum Hall effect terminates with a unique insulating phase. This phase is characterized by the divergence of the longitudinal resistivity with decreasing temperature, while the Hall resistivity remains quantized to its value in the last plateau. This phase remains a puzzle since the first studies from more than a decade ago [32, 33, 34, 35, 36, 37, 38, 39], as it contradicts all theoretical studies based on microscopically coherent quantum calculations [40, 41, 42, 43]. We demonstrate that these decoherence events stabilize the elusive quantum Hall insulator phase, which, in agreement with experiments, becomes even more stable with ans increasing temperature and voltage bias.

Chapter 1

Emergent Localized States in Length Tuned Quantum Point Contacts

As mentioned earlier quantum point contact (QPC) - a narrowing of the transport channel in two-dimensional electron gas(2DEG) heterostructure - is a basic nano-electronic device. When the transport is ballistic, the conductance is quantized to $2e^2/h * N$ [1] where e is the electron charge, h is Planck's constant, and N is the number of transverse modes in the QPC where the factor of two accounts for spin degeneracy. This can be understood within the non-interacting picture; nevertheless, even in the cleanest samples, there are deviations from this quantization due to electron-electron interactions[2, 3]. Despite extensive experimental and theoretical studies, full understanding of these anomalies is still an open problem.

1.1 Many Body Physics in Quantum Point Contacts

There are two signatures of many-body physics that are observed in QPC. First, there is an additional small plateau at the linear conductance trace at about $0.7 \cdot (2e^2/h)$ (0.7 anomaly). Second, the nonlinear differential conductance typically shows a peak around zero bias (Zero-

Bias Anomaly, ZBA) at conductance levels between quantized plateaus. Figure 1.1(a) shows linear conductance of QPC as a function of gate voltage for several temperatures. As the temperature increases, the shoulder around $0.7 \cdot (2e^2/h)$ becomes more visible, but the distinct plateau is less visible due to thermal smearing. Figure 1.1(b) shows the conductance for several in-plane magnetic fields. In a high magnetic field, the integer multiples are of e^2/h as the spin degeneracy is broken. Looking at the nonlinear differential conductance (Fig. 1.1), one can see the plateaus in the linear conductance as accumulation traces around zero bias. The similarity (lower region of Figs 1.1(e) and 1.1(f)) between the zero field at rather high temperatures and the high field $B = 8T$ nonlinear conductance data below $2e^2/h$, including the wing shape of the extra plateau that extends out from the 0.7 shoulder at zero field, suggests that this is a result of a splitting of spin bands, namely, a Zeeman splitting when a magnetic field is present. The low temperature data (left panel) show a narrow peak in the differential conductance around zero bias. This ZBA forms as the temperature decreases and is closely linked to the disappearance of the 0.7 shoulder at low temperatures; basically it raises the conductance toward the *unitary limit* $2e^2/h$.

These two signatures (Zero-Bias Anomaly and 0.7 anomaly) are reminiscent of the Kondo effect seen in quantum dots containing an odd number of electrons [4, 5, 6, 7, 8, 9, 10]. Indeed the scaling of the temperature dependence of the conductance fits with one scaling parameter designated as the Kondo temperature (Fig. 1.2). Moreover, this scaled curve is well described by a modified expression for the Kondo conductance:

$$g = 2\frac{e^2}{h}[\frac{1}{2f(T/T_k)} + \frac{1}{2}], \tag{1.1}$$

where $f(T/T_k)$ is a universal function for the Kondo conductance (normalized to $f(0) = 1$ well approximated by

$$f(T/T_k) \sim [1 + (2^{1/s} - 1)(T/T_k)^2]^{-s} \tag{1.2}$$

with s=0.22 [6]. Equation 1.1 differs from the one that has been previously used for quantum

dots [6] by the addition of constant e^2/h, which sets the high temperature limit to e^2/h, and by the fixing of the prefactor of $f(T/T_k)$ to 1/2.

Another feature of the Kondo regime ($T < T_k$) in quantum dots is that the zero bias peak is split by $2g^*\mu_B B$ with an in-plane magnetic field when $g^*\mu_B B >\sim T_K$. As can be seen in figure 1.2 (d), near the 0.7 shoulder, there is a splitting consistent with $2g^*\mu_B B$ up to $B \sim 3T$. At higher conductances, the two peaks merge since $g^*\mu_B B < T_K$. These similarities between quantum dots and QPC are quite surprising as QPC is an open system. This raises the question of from where does the Kondo physics in QPCs derive?

A SDFT calculation [44] of a single channel wire reveals the formation of a local moment with a net of one electron spin in the vicinity of the point contact. Later an extensive SDFT calculation [11] in a multi-channel wire in a hetro-structure revealed the formation of self-consistent or emergent localized states (ELSs), each having one electron charge inside the QPC. This theoretical work has led to the possibility that the many-body effects in QPC channels are intimately related to the occurrence of Friedel oscillations – oscillations in the electron charge density that occur when electron waves are reflected in a partially open QPC channel, which is enhanced into an ELS with about one electron of charge due to Coulomb repulsion and exchange interactions between electrons. The repulsion of electrons by the ELS (a precursor of the Coulomb blockade) can thus reduce the conductance, thereby explaining the observation of the 0.7 anomaly. In addition, transport through such a state can carry signatures of the Kondo effect [12], the most evident being the ZBA that emerges at temperatures below the Kondo temperature. At these temperatures which are, as noted, below a typical Kondo temperature, the conductance is enhanced by the Kondo effect, moving the 0.7 plateau towards $(2e^2/h)$, which is consistent with experiments. The theoretical work [11] has also predicted that, depending on parameters, a pair of such ELSs may emerge in the channel, resulting in a split peak ZBA, similar to that observed in double quantum dots [13], due to the double-impurity Kondo effect [14, 15, 16, 17].

It should be noted that these ELSs do not decay over time as their energy is below the Fermi

energy so that there are no unoccupied stated in the Fermi sea to decay to.

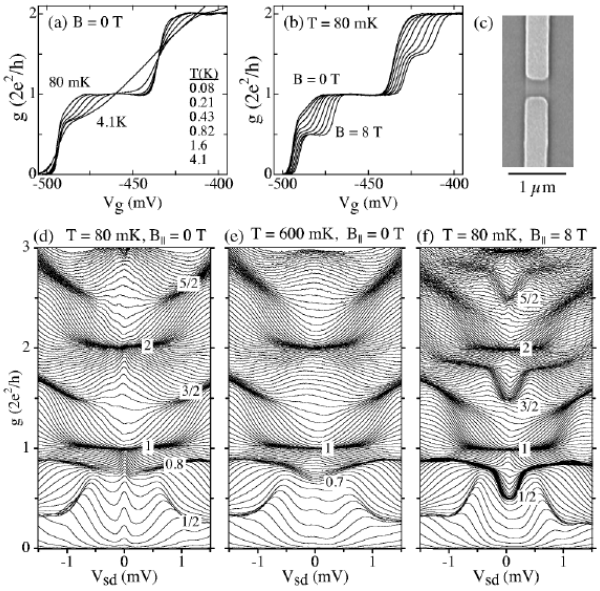

Figure 1.1: (a) Linear conductance ($g = dI/dV$, around $V_{sd} \sim 0$) versus gate voltage, V_g, at $B = 0$ for several temperatures. The extra plateau at $\sim 0.7 \cdot (2e^2/h)$ appears with increasing temperature while the plateaus at multiples of $2e^2/h$ become less visible due to thermal smearing. (b) Linear g versus V_g, for in-plane field B from 0 to 8 T in 1 T steps, showing spin-resolved plateaus at odd multiples of e^2/h at high fields. (c) Micrograph of the device reported. (d) (f) Nonlinear differential conductance $g = dI/dV$ as a function of dc source-drain bias voltage, V_{sd}, with each trace taken at a fixed gate voltage. Plateaus in $g(V_g)$ appear as accumulation of traces. (d) Nonlinear g at 80 mK, $B = 0$, at V_g intervals of 1.25 mV. Plateaus at multiples of $2e^2/h$ around $V_{sd} \sim 0$ and half-plateaus at odd multiples of e^2/h at high bias are visible. A zero-bias anomaly (ZBA) is present only at low magnetic field and low temperatures. At high bias, an extra plateau appears at $g \sim 0.8 \cdot (2e^2/h)$. (e) Nonlinear g at 600mK, $B = 0$, at V_g intervals of 1.0mV. Note absence of a ZBA and accumulation of traces at $g \sim 0.7 \cdot (2e^2/h)$ around $V_{sd} \sim 0$ that merge with the high-bias plateau at $g \sim 0.7 \cdot (2e^2/h)$. (f) Nonlinear g at 80mK, $B = 8T$, at V_g intervals of 1.2mV. Spin-resolved plateaus at odd multiples of e^2/h around $V_{sd} \sim 0$ merge with high-bias plateaus at $g \sim 0.8 \cdot (2e^2/h)$, and $g \sim 2.8 \cdot (2e^2/h)$. The high-bias feature at $g \sim 0.8 \cdot (2e^2/h)$ looks similar to that in the $B = 0$ data. Figure taken from [3].

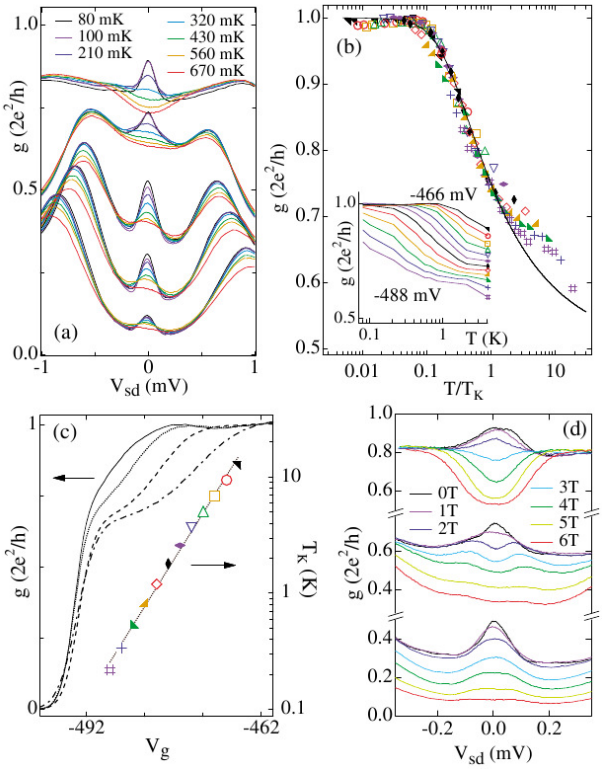

Figure 1.2: (a) Temperature dependence of the zero-bias anomaly (ZBA) for different gate voltages, at temperatures ranging between 80 and 670mK. (b) Linear g as a function of scaled temperature T/T_K where T_K is the single fit parameter in Eqs. (1.1), (1.2). Symbols correspond to gate voltages shown in inset. Inset: Linear conductance as a function of unscaled temperature, T , at several V_g . (c) T_K (right axis) obtained from the fits of $g(T/T_K, Vg)$ to Eqs. (1.1), (1.2), along with the conductance (left axis) at temperatures of 80 mK (solid line), 210 mK (dotted), 560 mK (dashed), and 1.6 K (dot-dashed). (d) Evolution of the ZBA with in-plane B, at V_g corresponding to high, intermediate, and low conductance. Splitting is clearly seen in the intermediate conductance data. Data in (d) were measured with zero perpendicular field. Figure taken from [3]

1.2 Experimental Results from Length-Tunable QPCs

Figure 1.3 presents novel 6-finger QPC_{6F} devices developed by the C. H. van der Wal group in Groningen [18], for which the channel length L_{eff} can be tuned continuously from about $186nm$ to $608nm$. These were operated with the gate voltage V_{g1} being always more negative

than V_{g2} to avoid quantum dot formation. By making V_{g1} less negative at fixed ratio V_{g2}/V_{g1} QPC channels are opened. The effective length L_{eff} is then set by V_{g2}/V_{g1} (short for V_{g2}/V_{g1} near 0, long for V_{g2}/V_{g1} near 1). The van der Wal group conducted electrostatic simulations (based on [45]) that show that the device operates in a regime where the gates induce a smooth saddle-point potential (Fig. 1.3B). That is, the narrow gaps between the gate fingers do not impose a significant structure on the potential.

Figure 1.3C presents linear conductance results for a QPC_{6F}. All QPC_{6F} showed clear quantized conductance plateaus. In addition, the 0.7 anomaly appears in most traces as a smaller plateau in the range 0.7 to $0.9(2e^2/h)$, and shows a dependence on L_{eff} for which three periods of modulation can be observed for the range $L_{eff} = 186nm$ to $608nm$. Nonlinear conductance measurements from this same device are presented in Fig. 1.4. Figure 1.4A shows how the ZBAs appear for $L_{eff} = 286nm$. At fixed length, the ZBAs alternate between a single-peak and double-peak characters when opening the QPC. Figure 1.4B shows that there is also a modulation between single- and double-peak characters when L_{eff} is increased at a fixed level for the conductance (as evaluated immediately next to the ZBA). Figure 1.4C plots again the data of Fig. 1.3C, with colored symbols on the traces that mark whether the ZBA at that point has single- or double peak character (in some cases, the ZBAs are best described as triple-peak). The modulation (in Fig. 1.3C.) between single-peak and double-peak ZBA as a function of L_{eff} also shows for about three periods, and is clearly correlated with the modulation of the 0.7 anomaly. Notably, the length increase of L_{eff} that induces one period of modulation ($100nm$ to $150nm$) has a value that matches with the Fermi wavelength in the QPC channel.

1.3 Spin Density Functional Theory Results

We have conducted an extensive SDFT (for explanation of SDFT, see appendix A) simulation to check the dependence of the number of ELSs on QPC length and gate voltage. These

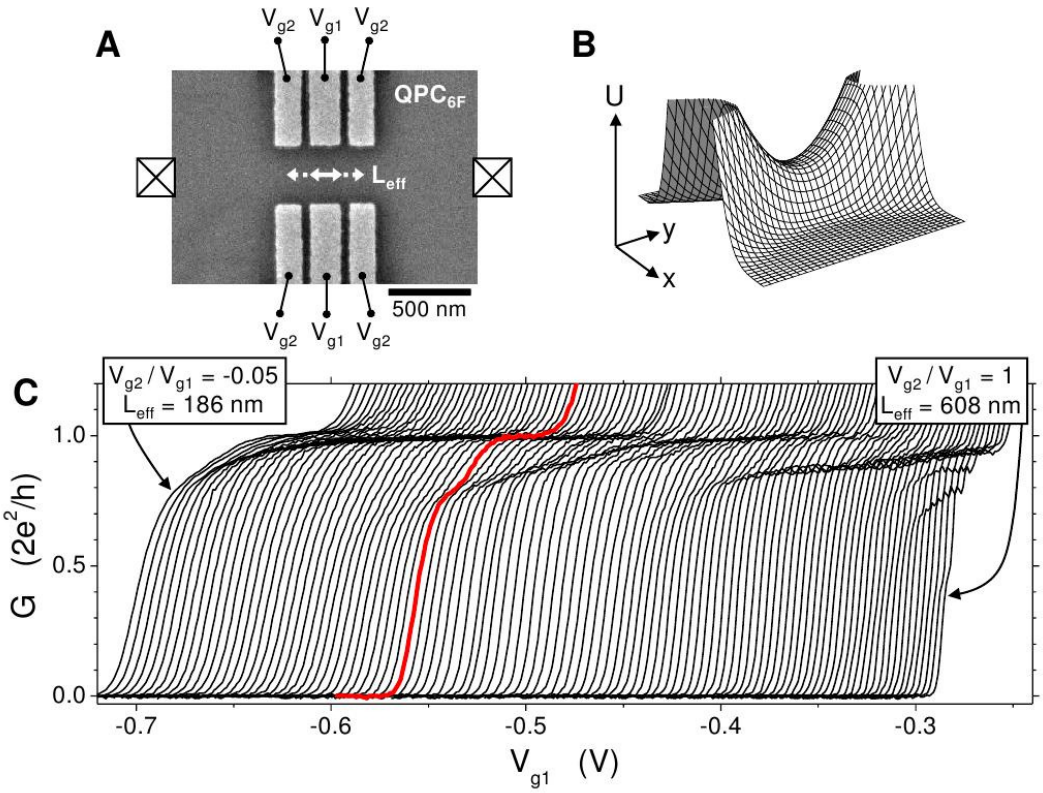

Figure 1.3: Length-tunable quantum point contact. **(A)** Electron microscope image of a QPC with 6 gate fingers (QPC_{6F}). It has a tunable effective length L_{eff} that is set by its operation at a fixed ratioV_{g2}/V_{g1}. **(B)** Saddle-point potential that illustrates the electron potential energy U (without many-body interactions) in the 2DEG plane in a QPC region. **(C)** Linear conductance G as a function of V_{g1} (while co-sweeping V_{g2} at fixed V_{g2}/V_{g1}) measured on a QPC_{6F} for L_{eff} tuned from 186 nm to 608 nm (traces not offset). Besides the quantized conductance plateau at $1 \cdot (2e^2/h)$, most traces show a smaller plateau in the range 0.7 to 0.9 $\cdot(2e^2/h)$ due to many-body effects. For this signature 3 periods of modulation can be observed in its dependence on V_{g2}/V_{g1} (i.e. L_{eff}).

simulations were carried out in a rectangular box (representing a piece of 2DEG), shown in Fig. 1.5, with periodic boundary conditions along the x-axis (horizontal in Fig. 1.5). The external potential is composed of a harmonic part $\frac{1}{2}\omega_y^2 y^2$, which represents the wire, and the QPC potential. The latter is calculated by placing two negatively-charged gate electrodes

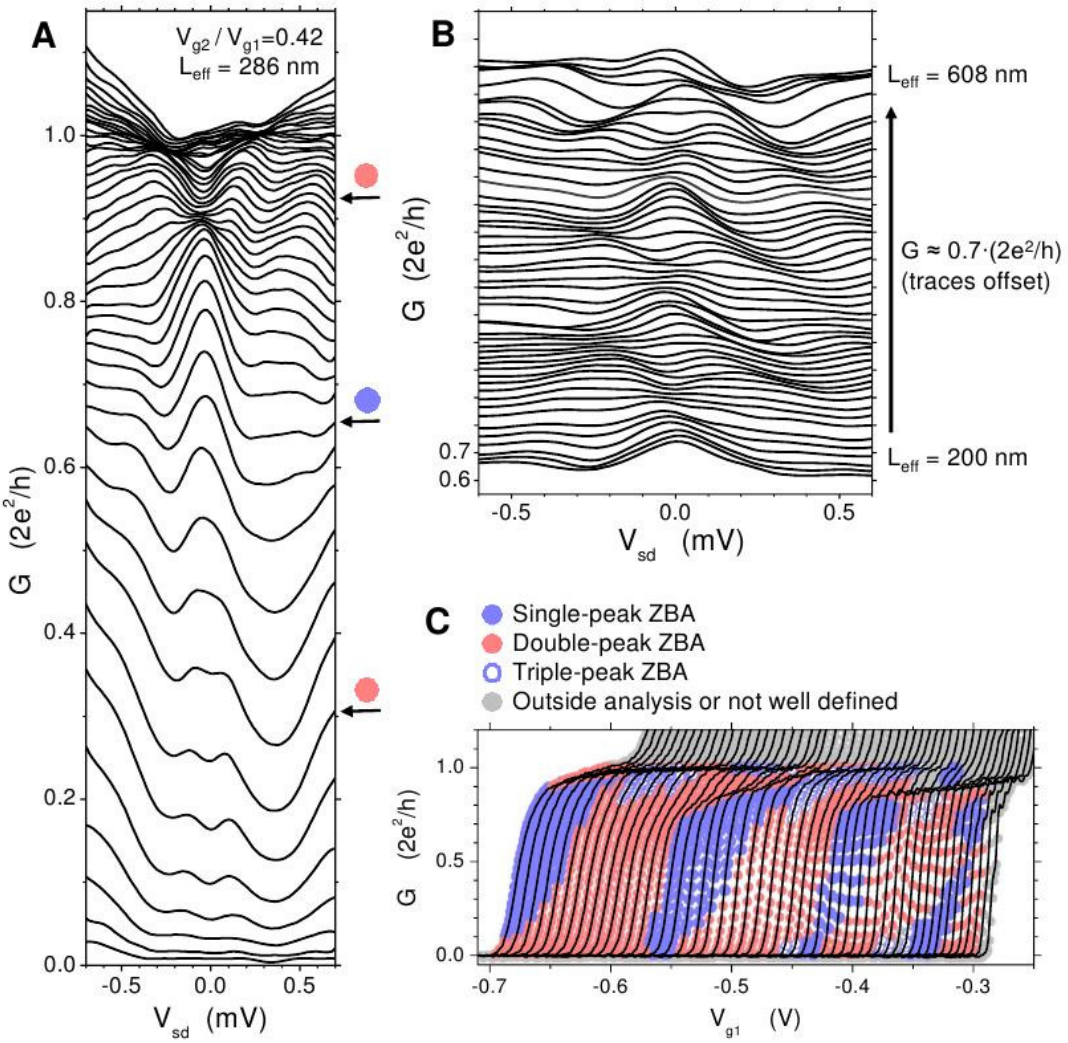

Figure 1.4: Zero-bias anomalies in the nonlinear conductance of a QPC_{6F} . **(A)** Nonlinear conductance G as a function of source-drain voltage V_{sd} at various V_{g1} settings, for operation at $L_{eff} = 286nm$. The ZBA appears alternatively with single- or double-peak character. **(B)** Evolution of the ZBA in the nonlinear conductance at fixed conductance level of $\sim 0.7 \cdot (2e^2/h)$ as a function of L_{eff} (traces offset). The ZBA has alternatively single- or double-peak character. **(C)** The character of the ZBA (single-, double-, or triple-peak, as labeled), mapped out on the linear conductance data of Fig. 1.3C.

at height $z_0 = 100$ nm above the 2DEG in the middle, using the Yukawa potential

$$v(\mathbf{x_0}, \mathbf{y_0}) = \int \rho_g \frac{e^{-|\mathbf{r}-\mathbf{r_0}|/\gamma}}{|\mathbf{r}-\mathbf{r_0}|} d\mathbf{r} \tag{1.3}$$

where $\mathbf{r_0} = \sqrt{x_0^2 + y_0^2 + z_0^2}$, $\gamma = 110$ nm and the integration is over the two-dimensional electrodes. The charge density of the electrodes ρ_g, is a linear function of the gate voltage on the electrodes $\rho_g = C_g V_g$ where C_g is the capacitance of the gate. In our simulation we set ρ_g, since C_g is unknown. The data is plotted vs the gate voltage V_g with arbitrary units.

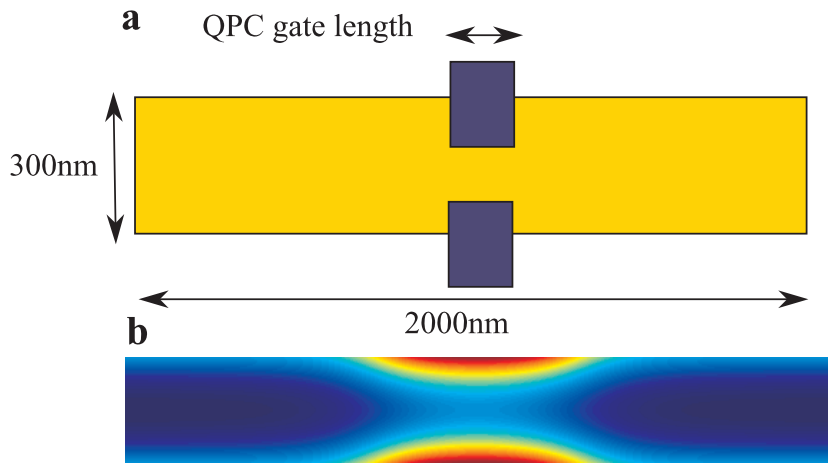

Figure 1.5: **(a)** Schematic of the simulation box; the blue rectangles represent the gate electrodes above the 2DEG. **(b)** Example of the external saddle-point and wire potential for a QPC (blue is lowest, red is highest potential).

For the Hartree term, we use the appropriate two-dimensional system with one-dimensional periodic boundary conditions [46]. In addition, we add a positive image charge plane at height 100 nm above the 2DEG as the contribution from the donor layer [44]. For the exchange and correlation functionals, we use the local-density approximation; for the exchange, we use the Slater exchange [47]; and the correlation functional is taken from quantum Monte-Carlo simulations of uniform electron gas [48]. The total number of electrons is $N = 108$ and the temperature is 300 mK (we have repeated some of the calculations with temperatures down

to 60 mK, with very little change in the results). We used the Octopus code [49] for solving the equations. For all the simulations, the electron effective mass $m_e^* = 0.067m_e$ and the dialectic constant $\kappa = 12.9$. The actual 2DEG electron density is slightly lower than in the experiments to keep the computational time of a simulation at a reasonable level, but we work in a regime where we capture the relevant physics. As a result, the relevant length scales (which are relative to the Fermi wavelength) are for the simulations also slightly longer than the experimental values.
The simulation steps are as follows:

- Set an external potential for a given QPC gate length and given gate voltage of the electrodes. In this simulation, opening the QPC is controlled with a single gate-voltage parameter V_g (in arbitrary units).

- Find the unpolarized ground state of the system by solving self consistently the Kohn-Sham equations.

- Polarize the solution by applying a magnetic field perpendicular to the sample (only the Zeeman term) for a few iterations, turn it off and lett the system flow to its ground state again (in this procedure we are basically giving an educated initial guess for the density). In principle, the field can be applied in any direction as it yields degenerate solutions.

- Repeat these steps for different QPC lengths and gate voltages.

Figure 1.6 shows two examples of the resulting densities; the left column is spin down density, while the right column is spin up density. The first is of unpolarized solution, then the spatially symmetric polarized solution, achieved by using a symmetric configuration of the magnetic field, and finally the spatially antisymmetric polarized solution achieved by using an antisymmetric configuration of the magnetic field.

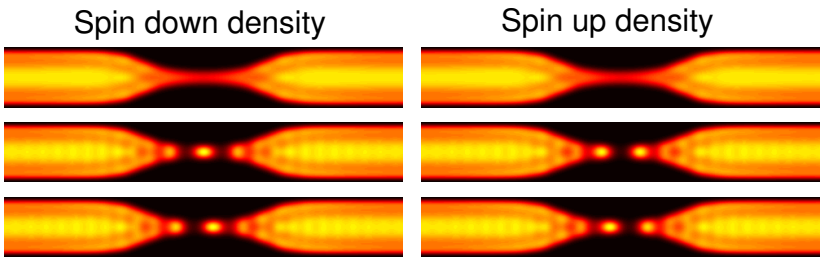

Figure 1.6: Spin-down (left) and spin-up (right) densities. Top row: unpolarized solution. Middle row: spatially symmetric polarized solution. Bottom row: spatially anti-symmetric polarized solution. The color scale extends from zero (black) to $2 \cdot 10^{14}$ m^{-2} (yellow).

The free energy difference between the polarized solutions relative to the unpolarized solution is shown in figure 1.7. When there exists a polarized solution, it has a lower energy than an unpolarized solution. Moreover, the spatially symmetric solution has a region $Vg = -[6.5 - 5.5]$ where it is the ground state of the system. In the following, we concentrate on this region, which is below the first plateau. The length of the QPC is deduced from the unpolarized solution by taking the length of the channel between the two points of density 80% of the maximum density as depicted in figure 1.7. As mentioned earlier, the emergent localized states (ELSs) inside the QPC originate from Friedel oscillations and as the QPC becomes longer, the Friedel oscillations have more periods inside the QPC channel. We use two complementary procedures in order to determine the number of ELSs inside the QPC. First, we look at the cross-section of the density across the middle of the sample (this is done separately for spin up density and spin down density). The criteria for the definition of the peaks is given by

$$n_\sigma(\mathbf{r}_{max}) * P \geq n_\sigma(\mathbf{r}_{min}), \tag{1.4}$$

where n_σ is the density of spin σ, and $\mathbf{r}_{min}$ is the closest minimum toward the outside of the QPC. This procedure is shown in figure 1.8 for $P = 0.32$. As can be seen in the figure, this

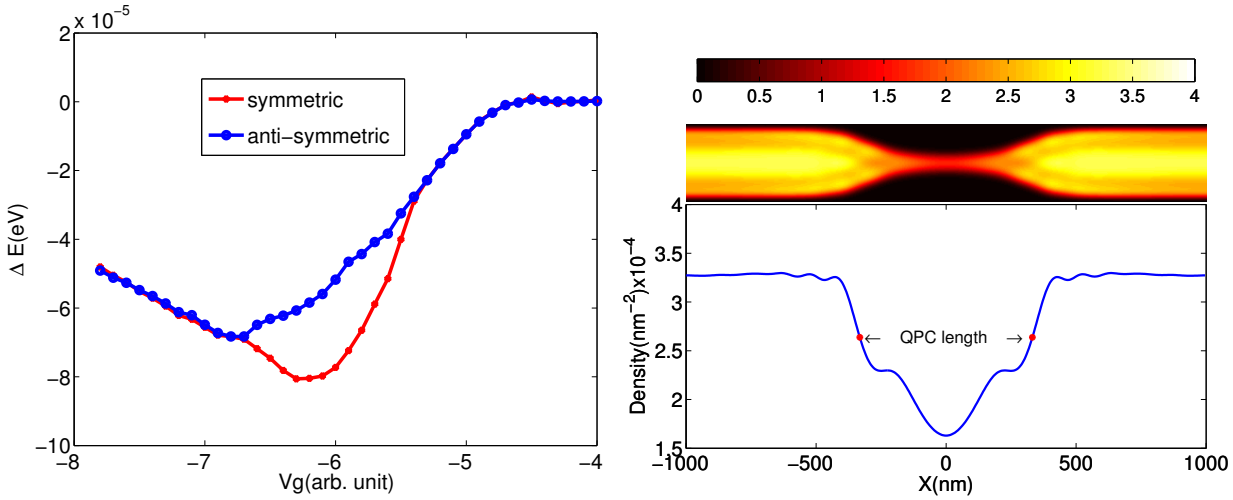

Figure 1.7: Right: Free energies of the symmetric and anti-symmetric polarized solutions relative to the unpolarized solution as a function of gate voltage, for a QPC length of 680 nm. Left: QPC length calculation.QPC length calculation. The blue line is a cross-section of the total density across the middle of the QPC channel. Above is the total electron density zero (black) to $3.5 \cdot 10^{14}$ m^{-2} (yellow). The red dots mark the density at 80% of the maximum density.

procedure may be problematic when the solution is ferromagnetic, and the peaks overlap significantly. In such cases, we use a second procedure: An example is given in Fig 1.9. The total two-dimensional spin up density (B) can be fit to a sum of five Gaussians (only three of them inside the QPC), each of the total unit weight, even though the cross-section reveals only two peaks inside the QPC.

Our main result is summarized in figure 1.10B, where we show for each gate-voltage and QPC length the number of ELSs in the ground state. In fig 1.10A we show how this number increases with length for a fixed gate voltage, for each additional Fermi wave length inside the QPC (150 nm in the bulk) there is additional ELS. This is in agreement with what was shown above, that the change in the number of ELSs is driven by additional periods of Friedel oscillations that form in the QPC as it gets longer. While the number of ELSs inside the QPC may depend on how we define the extent of the QPC, its parity is independent

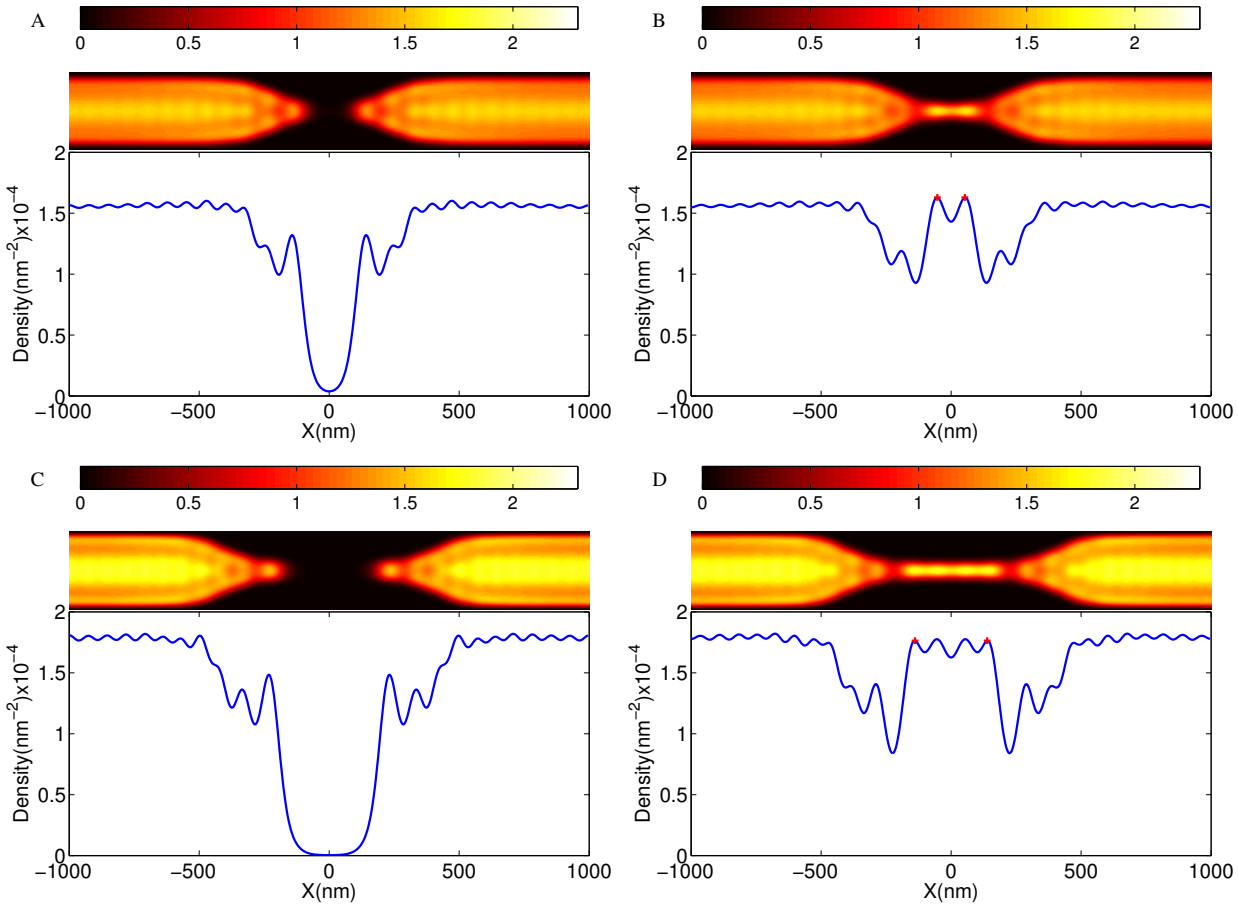

Figure 1.8: Example for counting ELSs - first method. **(A,B)** Electron density and its cross-section for spin up (A) and spin down (B) at $V_g = -6$ and for $L = 540$ nm. The red crosses mark the Friedel oscillations that are counted as ELSs. Here we have a total of two ELSs in the QPC, each one with a density very close to one electron. **(C,D)** Electron density and its cross-section of spin-up (C) and spin-down (D) densities at $V_g = -6$ and for $L = 830$ nm. In this case, there are four ELSs, as can be seen from the cross-section.

of that choice. This parity defines the character of the Kondo effect, for example: taking a longer QPC in Fig. 1.9 will add two ELSs – the cyan Gaussians – inside the QPC, and will not change the parity.

The oscillations of the parity in the number of ELSs inside the QPC support the picture we have presented above. When there is anodd number of ELSs we expect to see zero bias

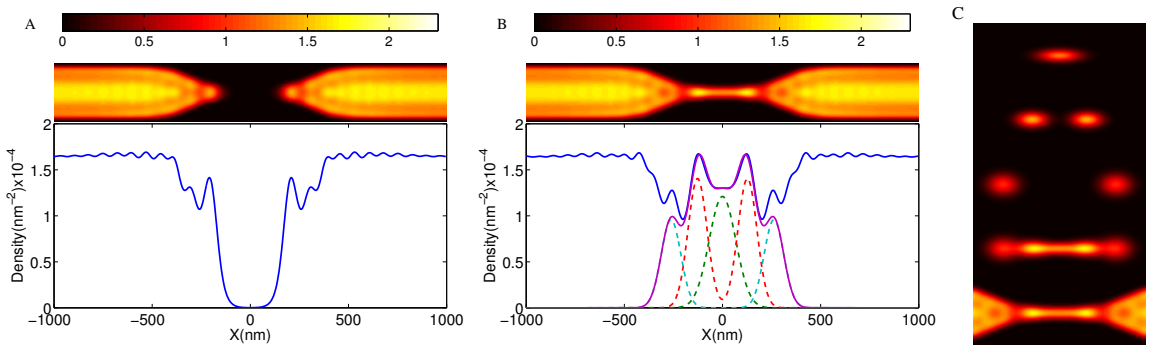

Figure 1.9: Example for counting ELSs - method 2. **A** (B) Electron density and its cross-section of spin up (down) at $Vg = -6$ and $L_{eff} = 680nm$; here the integration of the density inside the QPC gives a total of three electrons, though there are only two peaks in the cross-section.The two-dimensional density can be fitted to a sum of 5 unit weight Gaussians, three of which are in the QPC. **(C)** We show how the five Gaussians give the corresponding SDFT density. From top to bottom: Center Gaussian (corresponds to green dashed line in the cross-section), two nearest Gaussians (red dashed line), two next nearest Gaussians (cyan dashed line), all five Gaussians together (purple line), SDFT density (blue line). Hence we conclude that there are three localized ELSs inside the QPC.

peak in the differential conductance as observed in a single quantum dot. In the case of an even number of ELSs we expect to see a split peak in the differential conductance as seen in coupled double quantum dots [50, 13].

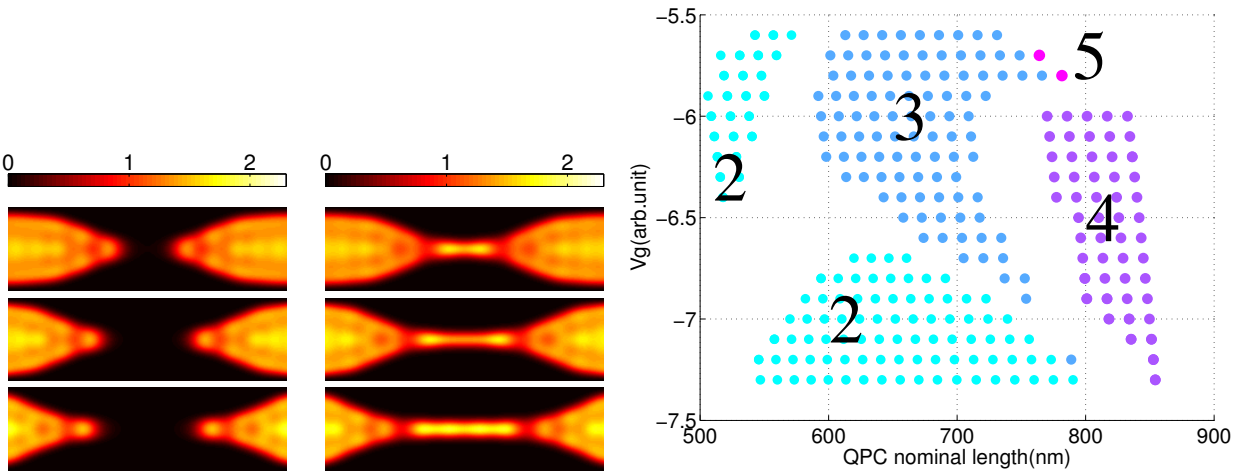

Figure 1.10: **A.** Polarized electron density for spin up right panel (down left panel) at constant gate voltage $V_g = -6$ for three different lengths (540nm, 680nm and 830nm), the number of ELSs inside the QPC is two, three and four respectively. The number of ELSs increases by one for each additional Fermi wave length (150nm in the bulk) inside the QPC. The color scale extended from zero (black) to $2 \cdot 10^{14}\ m^{-2}$ (yellow). **B.** Number of ELSs inside the QPC as a function of gate voltage and QPC length.

1.4 Conclusion

Our numerical SDFT modeling, which also accounts for Coulomb and exchange interactions, showed that Friedel oscillations generically develop into ELSs whose number grows with the QPC length, leading to alternating parity that is consistent with a periodic modulation between single-peak and double-peak ZBAs. In turn, with such localized states near a reservoir, the Kondo effect will often play a role in the formation of the many-body state. Past research on quantum has dots showed that, under these conditions, the Kondo effect is a very generic phenomenon while the behavior of the ZBAs in QPCs show a strong correspondence with transport through single and paired Kondo states. We showed that the periodic character of both the ZBA and the 0.7 anomaly as a function of QPC length provides evidence that the physics of Friedel oscillations is fundamental to these phenomena.

Chapter 2

Dephasing in Two-Dimensional Disordered Systems

Coherence time, the time over which the phase of the wave function is maintained, is one of the fundamental properties in quantum mechanics, and is especially important for mesoscopic systems where the coherence length is of the order of the sample size. From basic quantum mechanical arguments one expects that as the temperature goes down, the external degrees of freedom freeze out, so that the coherence time will be infinite at zero temperature. For temperatures less than one Kelvin, the phonon's contribution to dephasing becomes negligible and the main processes of dephasing are due to electron-electron interactions. From theory [19, 20], one expects a power law dependence of the dephasing rate on the temperature, which was confirmed in experiments at that temperature range. However, when the temperature is decreased further, there is apparent saturation in the coherence time [21, 22, 23, 24, 25, 26, 27, 28, 29] (see, as an example figure, 2.1) which is in contradiction with the electron-electron interaction picture, and possibly with the general quantum mechanical principle described above. One possible explanation for this saturation is magnetic impurities: At temperatures higher than the Kondo temperature, there is a fi-

nite probability for spin flip scattering that will cause dephasing. Follow-up experiments [28] have demonstrated that a small amount of magnetic impurities changes the temperature dependence of the phase coherence time τ_ϕ from a power law to saturation at low temperatures as depicted in figure 2.2. However, the conductors of the original experiments [26] claim that they checked and found that no magnetic impurities exist in their system. Moreover, one does not expect any magnetic impurities in semi-conductor systems, where the same effect has also been seen [22, 23, 24, 27].

It has been shown in another context [44, 11] [and in chapter 1 of this thesis] that a magnetic moment forms at the saddle-point of a potential in single and multi-channel wires in heterostructure. Since QPCs form naturally at the saddle-points of a two-dimensional disordered systems, one can ask: Can these magnetic moments be formed in a two dimensional disordered systems? And, if so, are they responsible for the saturation of the coherence time?

2.1 Theoretical Models

Dephasing Processes

In the presence of several decoherence mechanisms, the phase coherence time τ_ϕ is expressed by

$$\frac{1}{\tau_\phi} = \frac{1}{\tau_{\mathrm{e-ph}}} + \frac{1}{\tau_{\mathrm{e-e}}} + \frac{2}{\tau_{\mathrm{mag}}} + \cdots . \tag{2.1}$$

At relatively high temperatures, the leading contribution to dephasing is from electron-phonon interactions. The temperature dependence of coherence time due to this inelastic process is given by [51]

$$\frac{1}{\tau_{\mathrm{e-ph}}} \sim T^3. \tag{2.2}$$

For temperatures below 1 K, the phonons are suppressed and thus their contribution to dephasing processes is diminished. At these temperatures, the main source of decoherence

arises from small energy transfers between electrons due to electron-electron interactions [19] (dubbed the AAK term)

$$\frac{1}{\tau_{\mathrm{e-e}}} = \left(\frac{T}{D^{d/2}\nu_d\hbar^2}\right)^{2/(4-d)}; \tag{2.3}$$

here d is the dimension, D is the diffusion coefficient and ν_d is the density of states. For the quasi-1D disordered systems, we obtain

$$\frac{1}{\tau_{\mathrm{e-e}}^{\mathrm{1D}}} = \frac{1}{2}\left(\frac{k_B\pi}{wm^*}\right)^{2/3} D^{-1/3}T^{2/3}, \tag{2.4}$$

where k_B is the Boltzmann constant, m^* is the effective mass of the electron and w is the width of the wire. For the 2D case, one obtains

$$\frac{1}{\tau_{\mathrm{e-e}}^{\mathrm{2D}}} \simeq \frac{k_BT}{2m^*D}\ln\left(\frac{2m^*D}{\hbar}\right). \tag{2.5}$$

In the presence of magnetic impurities, the dephasing rate has an additional contribution resulting from electrons that are scattered off these magnetic impurities. For temperatures higher than the Kondo temperature $T > T_K$, the temperature dependence of the coherence time is given by the Nagaoka-Suhl (NS) expression [52] as

$$\frac{1}{\tau_{\mathrm{mag}}} = A\frac{\pi^2S(S+1)}{\pi^2S(S+1)+ln^2(T/T_K)}c_{imp}, \tag{2.6}$$

where S is the spin of the impurity, A is the prefactor in units of 1/s, and c_{imp} is the magnetic impurities concentration. At the opposite limit ($T \ll T_K$), Nozieres Fermi liquid theory predicts a T^2 dependence of the inelastic scattering rate from an $S = 1/2$ impurity when the screening is complete [53]. For a spin larger than one, the screening is incomplete and the low temperature behavior is given by [54],

$$\frac{1}{\tau_{\mathrm{mag}}} \sim \frac{S^2-1/4}{ln^2(T/T_K)}. \tag{2.7}$$

Recently, Zarand *et al.* were able to obtain an exact solution for the inelastic scattering time in Kondo metals using Wilson's numerical Renormalization-Group(NRG) calculation,

ranging from zero temperature to well above Kondo temperature [55]

$$\frac{1}{\tau_{\rm mag}} = B\frac{\sigma(w)_{inel}}{\sigma_0}c_{imp}, \tag{2.8}$$

where $\sigma(w)_{inel}$ is the inelastic scattering cross-section at finite energy w, $\sigma_0 = 4\pi/k_f^2$ is the elastic scattering cross-section at zero temperature, and B is a numerical constant.

Weak Localization

The quantum nature of electrons leads to constructive interference between time-reversed paths, thus reducing the probability of an electron reaching the other end of the sample and therefore increasing resistivity. The correction of the classical conductivity for diffusive electrons due to interference is given by

$$\frac{\delta\sigma}{\sigma} \simeq -\int_{\tau}^{\tau_\phi} \frac{v_F\lambda_F^{d-1}}{(Dt)^{d/2}}dt \tag{2.9}$$

where v_F, λ_F are Fermi velocity and wave length, respectively and d is the dimension of the system. The lower limit of the integration τ is the mean free time between elastic collisions, and the upper limit τ_ϕ is the phase coherence time. For longer times, interference is no longer relevant. Equation 2.9 depends on the phase coherence time τ_ϕ or, alternatively, on the phase coherence length $L_\phi = \sqrt{D\tau_\phi}$. This correction to the conductivity depends on the magnetic field, which destroys constructive interference between the time-reversed paths due to the additional Aharonov-Bohm phase. In the experiment one measures the changes in conductivity as a function of the magnetic field, fits the results to the theory and, from that extracts the coherence time.

2.2 Experimental Evidence

Mohanty *et al.* [26] report an extensive set of experiments designed to understand the temperature dependence of τ_ϕ as temperature decreases. They fabricated six quasi-1D pure

gold wires with less than 1 ppm of magnetic impurities, in different lengths, widths and thicknesses. Using a weak-localization measurement (WL) and fitting the results to the standard 1D form [56], they deduced the phase coherence length L_ϕ. The coherence time was then obtained by $\tau_\phi = L_\phi^2/D$, where D is the classical diffusion coefficient. Panel a in figure 2.1 shows the temperature dependence of τ_ϕ from 11 mK to 7 K below 200 mK, the temperature dependence of τ_ϕ is slower than expected from theory [19] and seems to saturate below 40 mK. The effect of magnetic impurities on τ_ϕ was also studied by Fe ion implanting, the dominant magnetic impurity in Au. Fig. 2.1b displays temperature dependence of τ_ϕ for the same sample before and after the ion implanting. The effect of adding magnetic impurities is to lower the magnitude of the phase coherence time, but not to cause saturation in τ_ϕ, in accordance with previous experiments [57, 58]. Moreover, the saturation of τ_ϕ also exists in semiconductor wires [22, 23, 24, 27], which are not supposed to contain magnetic impurities. The conclusion of the authors of [26] is that the saturation of the coherence time is not due to heating, magnetic impurities, or external environmental effects.

In a later study, Pierre *et al.* [28] again used WL measurement in order to find the coherence time τ_ϕ in very clean copper (Cu), silver (Ag) and gold (Au) wires. Though some of the samples have comparable resistances and geometries similar to those of some of the samples used in [26], the low temperature behavior of τ_ϕ is different and so are the conclusions of the authors. Panel a of figure 2.2 shows τ_ϕ as a function of temperature for samples Ag(6N),Ag(5N),Au(6N) and Cu(6N), where 5N and 6N are samples of purity of 10 ppm and 1 ppm respectively. The samples Ag(6N)and Au(6N) have larger τ_ϕ and keep increasing, which is according to the theory of electron-electron interactions, while Ag(5N) and Cu(6N) samples show smaller τ_ϕ and saturation at low temperatures. The different behavior of the two silver samples shows that τ_ϕ is related to the purity of the sample. The authors suggest several possibilities for the source of dephasing, two of which are very dilute magnetic impurities or dephasing from two-level systems associated with lattice defects. As for the copper wires, there is always weak temperature dependence below 200 mK regardless of

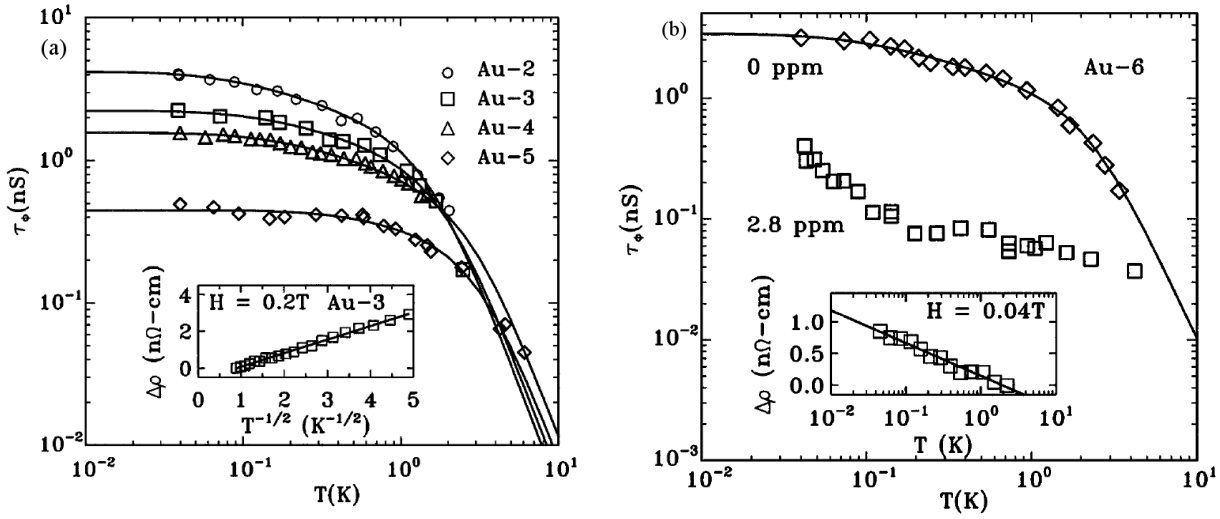

Figure 2.1: **(a)** Temperature dependence of τ_ϕ for four Au wires. Solid lines are fits to theory (Eq. 1 of Ref. [26]). The inset is the EE contribution to $\Delta\rho$ compared to the theoretical prediction. **(b)** Temperature dependence of τ_ϕ before (diamonds) and after (boxes) Fe implantation. The solid line is a fit to theory (Eq. 1 of Ref. [26]). The inset shows the dependence of $\Delta\rho$ due to magnetic impurities with a theoretical fit. From Ref [26].

the purity of the sample. They attribute this to the surface oxide of copper, which can cause dephasing [59]. In order to check whether spin flip scattering is responsible for the saturation of τ_ϕ at low temperatures, Pierre *et al.* fabricated three silver samples of Ag(5N) with very dilute manganese atoms (0.3 ppm and 1 ppm). The phase coherence times are shown in Fig. 2.2b together with reference samples of Ag(6N) and Ag(5N). The samples with the manganese impurities exhibit smaller τ_ϕ and weak temperature dependence at low temperatures.

Given the NRG theoretical results [55], Bäuerle *et al.* [29], compared the temperature dependence of τ_ϕ with this theory. First they looked at the coherence time of gold wires with iron impurities with a concentration of 3.3 ppm and 45 ppm (shown in the left panel of figure 2.3). As one can see, the NRG calculation is a good fit with experimental data for the low temperatures where the Nagaoka-Suhl expression (Eq. 2.6) is not valid. After establishing

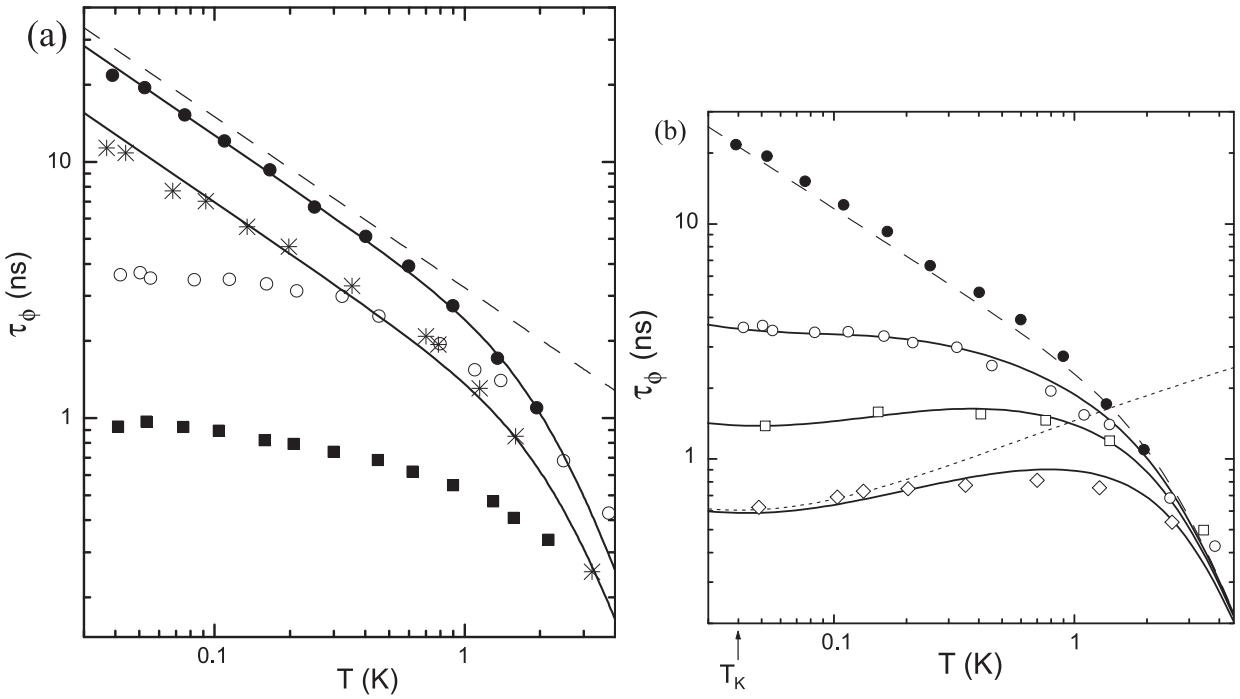

Figure 2.2: **(a)** Phase coherence time τ_ϕ versus temperature in wires made of copper Cu(6N) (■), gold Au(6N) (∗), and silver Ag(6N) (•) and Ag(5N) (○). The phase coherence time increases continuously with decreasing temperature in wires fabricated using the purest (6N) silver and gold sources as illustrated respectively with samples Ag(6N) and Au(6N). Continuous lines are fits of the measured phase coherence time including inelastic collisions with electrons and phonons. The dashed line is the prediction of electron-electron interactions only for sample Ag(6N). In contrast, the phase coherence time increases much more slowly in samples made of copper (independently of the source material purity) and in samples made of silver using a source of lower (5N) nominal purity. **(b)** Phase coherence time as function of temperature in several silver wires. Sample Ag(6N)c (•) is made of the purest silver source. Samples Ag(5N) (○), $\mathrm{Ag(5N)_{Mn0.3}}$ (□) and $\mathrm{Ag(5N)_{Mn1}}$ (⋄) were evaporated simultaneously using the 5N silver source. Afterward, 0.3 ppm and 1 ppm of manganese was added by ion implantation respectively in samples $\mathrm{Ag(5N)_{Mn0.3}}$ and $\mathrm{Ag(5N)_{Mn1}}$. From Ref [28].

that the NRG theory describes rather well the temperature dependence of τ_ϕ, the authors looked at the τ_ϕ of a very clean gold wire with less than 0.015 ppm of impurities at very low temperatures (as low as 0.01 K). Surprisingly, at these low temperatures there is again

saturation (or weak temperature dependence) of the coherence time, as shown in the right panel of figure 2.3. To check whether this saturation can be explained by the presence of very dilute magnetic impurities, a comparison with the NRG theory was made for different impurity concentrations and Kondo temperatures. As can be seen in the right panel of the figure, the best fit of the theory with experimental data is for impurities with a concentration of 0.015 ppm with Kondo temperature $T_k = 5mK$. A possible magnetic impurity with Kondo temperature in this range is manganese ($T_k \simeq 3mK$). However, the dominant magnetic impurity in gold is iron, so one should expect, in addition to the manganese, at least 0.015 ppm of iron ($T_k \simeq 500mK$). Judging from the comparison with the NRG calculation regarding these two impurities (dotted line), the fit is less satisfactory. This may suggest that extrinsic magnetic impurities are not responsible for the apparent saturation of τ_ϕ at low temperatures.

In a recent study of the disorder dependence of the phase coherence time of quasi one-dimensional wires and two-dimensional 2D Hall bars fabricated from a high mobility heterostructure [60], it was found that the intrinsic disorder in the 2D electron gas can be changed through the ion implantation technique. The Ga^+ or Mn^+ ions are implanted $50nm$ above the 2DEG in the desired concentration. In a diffusive regime, the phase coherence length follows a power law as a function of the diffusion coefficient (as expected from Fermi-liquid theory see figure 2.4), without any sign of low-temperature saturation. In a strongly localized regime, a diverging phase coherence time was found when the temperature was decreased, although with a smaller exponent compared with a weakly localized regime (see figure 2.5).

These observations motivated us to study the possible mechanism of spontaneous formation of magnetic impurities due to disorder.

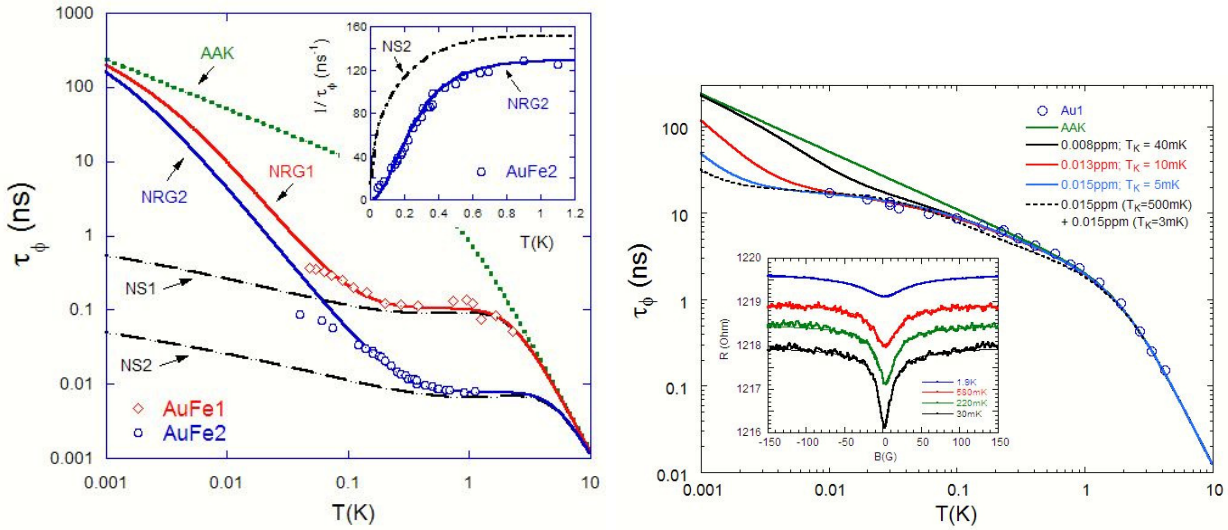

Figure 2.3: Left: Phase coherence time as a function of temperature for two Au/Fe Kondo wires: $\diamond$ sample with 3.3 ppm iron impurities , $\circ$ sample sample with 45 ppm iron impurities. The green dotted line (denoted AAK) corresponds to the assumption that only electron-electron and electron-phonon interaction contribute to dephasing. The black dashed-dotted lines (NS1 and NS2) take in addition account for the magnetic scattering using the NS expression, whereas for the red (NRG1) and blue (NRG2) solid lines, the NRG calculation has been employed for the contribution of the magnetic impurities. Right: Phase coherence time as a function of temperature for sample Au1 ($\circ$). The solid green line corresponds to the AAK prediction, the black (a), red (b) and blue (c) solid lines correspond to the NRG calculation assuming $T_K = 40\,\mathrm{mK}$, $T_K = 10\,\mathrm{mK}$, and $T_K = 5\,\mathrm{mK}$, respectively. From Ref [29].

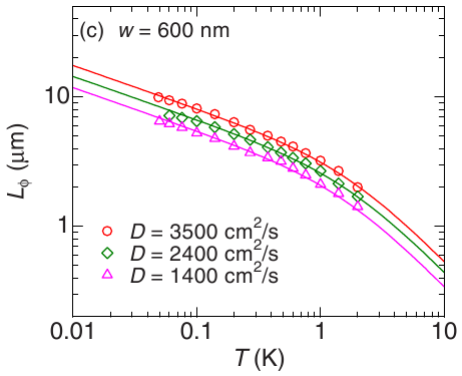

Figure 2.4: Phase coherence length L_ϕ as a function of T at several different diffusion coefficients. The phase coherence length follows a power law as a function of diffusion coefficient as expected in the Fermi-liquid theory (solid line) . Taken from [60].

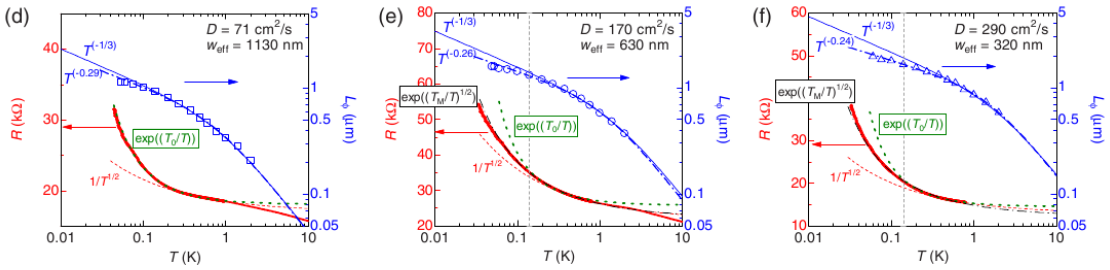

Figure 2.5: (d)-(f) Experimental data of $R(T)$ (red solid lines) and L_ϕ (blue open symbols) as a function of T; (d) $w_{\rm eff} = 1130$, (e) 630 and (f) 320 nm. The solid lines for L_ϕ(T) are the best fits of Eq. (2.4). The dashed-dotted lines, represent a change in the exponent of $L_\phi(T)$ at the low temperature part from $-1/3$ (AAK) to -0.29 ($w_{\rm eff} = 1130$ nm), -0.26 ($w_{\rm eff} = 630$ nm) or -0.24 ($w_{\rm eff} = 320$ nm) in order to get better fitting precisions a lower temperatures. Taken from [60].

2.3 Spin Density Functional Theory Results

Our SDFT simulation was carried out in a two-dimensional square box with periodic boundary conditions. The disorder external potential was composed of point-like changes at different distances above the sample plane that mimic remote impurities or defects in the lattice. Their contribution to the external potential of the SDFT simulation is given by the Yukawa potential

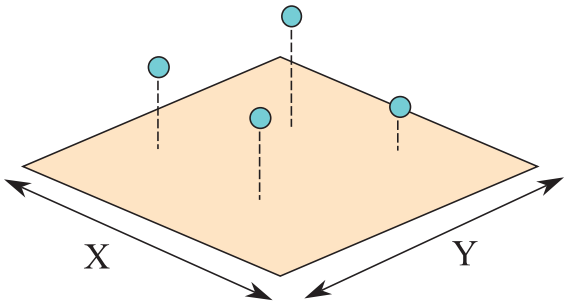

Figure 2.6: Scheme of the simulation box, the cyan dots represent point-like changes at different distances above the sample plane

$$v(\mathbf{x_0}, \mathbf{y_0}) = \sum_i C_i \frac{e^{-|\mathbf{r_i}-\mathbf{r_0}|/\gamma}}{|\mathbf{r_i}-\mathbf{r_0}|}, \tag{2.10}$$

where $\mathbf{r_0} = \sqrt{x_0^2 + y_0^2}$, $\mathbf{r_i} = \sqrt{x_i^2 + y_i^2 + z_i^2}$, $\gamma = 90nm$, and C_i is the charge. For the Hartree term, we use the appropriate two-dimensional system with two-dimensional periodic boundary conditions [46]. For the exchange and correlation functionals, we use the local density approximation. For the exchange we use the Slater exchange [47]. The correlation functional is taken from quantum Monte-Carlo simulations of a uniform electron gas [48]. For all the simulations, the electron effective mass $m_e^* = 0.067m_e$ and the dialectic constant $\kappa = 12.9$. We use the Octopus code [49] for solving the equations.

The simulation steps are as follows:

- Set an external potential for a given disorder.

- Find the unpolarized ground state of the system by solving self-consistently the Khon-Sham equations.
- Polarize the solution through the application of a magnetic field perpendicular to the sample (only Zeeman term) for a few iterations. Turn it off and lett the system flow to its ground state again.[1] The magnetic field can be applied locally.
- Repeat these steps for different disorder configurations, densities and temperatures.

We start by studying the properties of a one saddle-point potential, created from two impurities of one electron charge at height 10nm above the 2DEG. Figure 2.7(a) shows the external potential of such a configuration with a distance of 120nm between the impurities. The spin up and down densities are shown in panel (c) and (d) respectively. Looking at polarization, $n_{\uparrow}[\mathbf{r}] - n_{\downarrow}[\mathbf{r}]$, shown in Fig 2.7(b), there is excess of spin up density, emergent localized state (ELS), at the saddle-point of the external potential.

Figure 2.8(a) shows the magnitude of the ELS, M (see figure 2.7b), inside the saddle-point as a function of d, the distance between the two impurities, at temperatures of 100, 150 and 200mK. The maximal magnitude of the ELS is at $x = 108nm$, Fig. 2.8(c) depict the temperature dependence of M. We can see that the ELS magnitude increases as the temperature decreases and saturates at 40mK. In all the cases the polarized solution free energy is lower than the non-polarized solution (δE in Fig 2.8(c,d)).

Figure 2.9 shows the ELS magnitude as a function of strength of the external potential, (we do so by changing the impurity charge), for different electron densities. As the density gets higher, a stronger potential is needed to form an ELS.

[1] Basically, in this procedure we are giving an educated initial guess for the density.

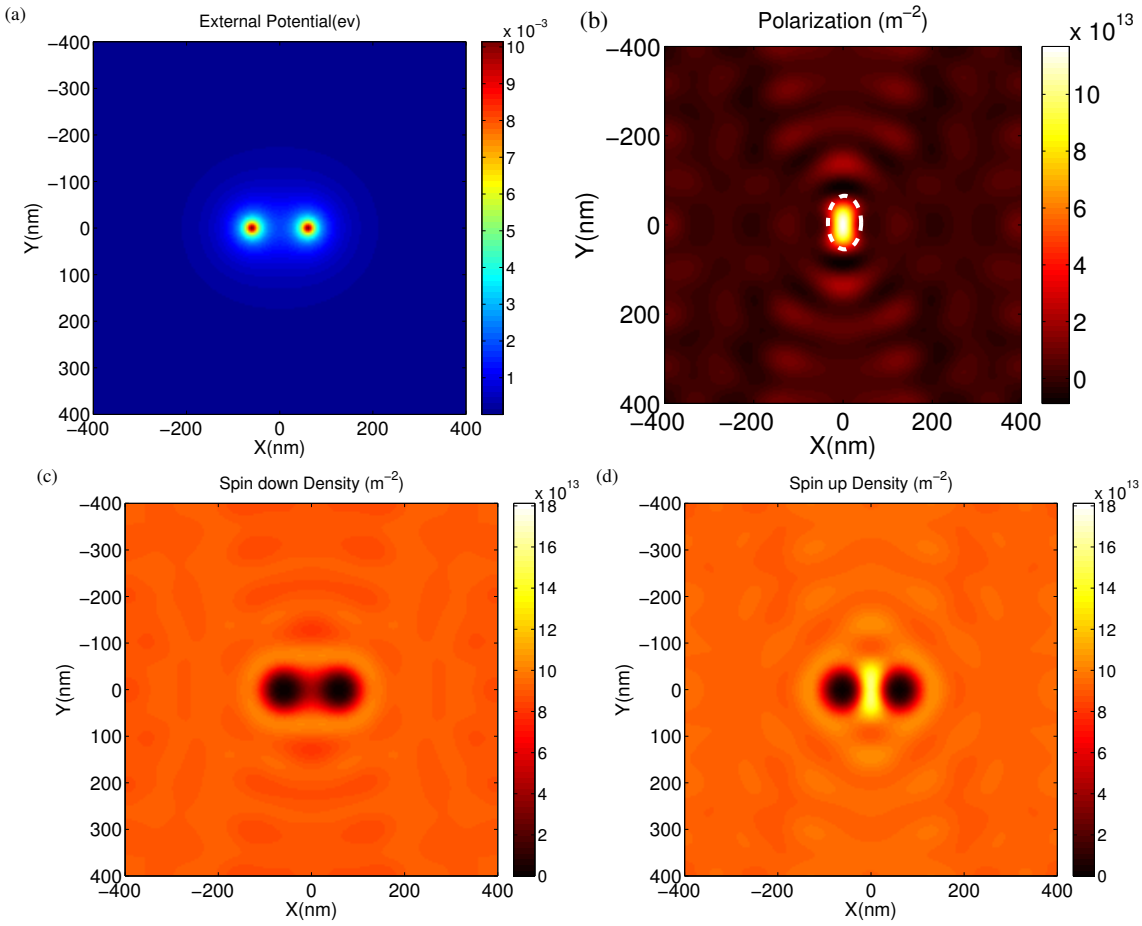

Figure 2.7: **(a)** One saddle-point potential, created from two impurities of one electron charge at height 10nm above the 2DEG, the distance between them is 120nm, with charge of one electron and $\gamma = 90$ (see Eq. 2.10). **(b)** Polarization density $n_\uparrow[\mathbf{r}] - n_\downarrow[\mathbf{r}]$. In order to determine the magnitude of the ELS, M, we integrate the polarization density over the region enclosed by dashed white ellipse, $M = 0.6$ in this example. **(c)** Spin down density. **(d)** Spin up density.

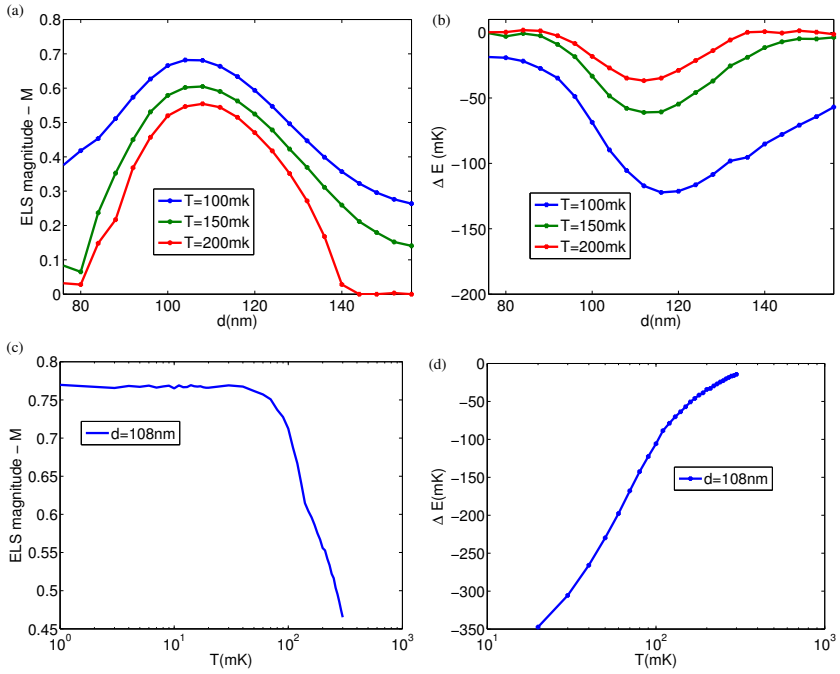

Figure 2.8: One ELS properties: **(a)** magnitude of the ELS as a function of d, the distance between the two impurities that create the saddle point potential, for three different temperatures. **(b)** free energy of the polarized state relative to the non-polarized solution, ΔE, as a function of d for three different temperatures. **(c)** ELS magnitude, M, as a function of temperature for d=108nm. **(d)** ΔE as a function of temperature for d=108nm, there is no data below 20mK due to convergence problems of the non-polarized solutions at such low temperatures.

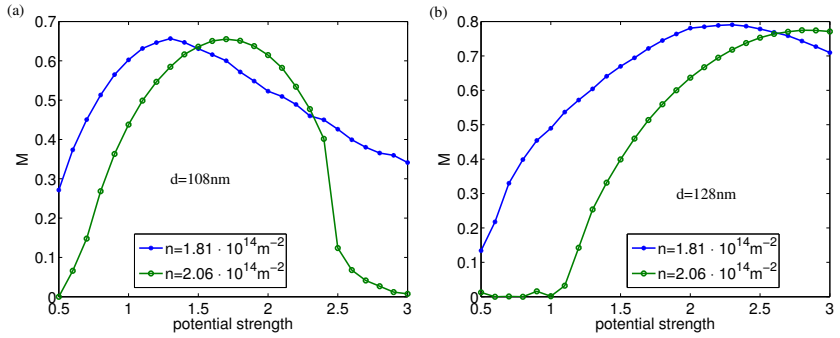

Figure 2.9: One ELS properties: ESLs magnitude, M, as a function of strength of the external potential for two densities, the length between the impurities is 108nm (a) and 128nm (b). At higher densities a stronger external potential is needed to form ELS.

In order to see whether there is correlation between the ELSs we consider two saddle-points potential as shown in figure 2.10(a). The free energy differences between the non-polarized solution and the polarized solutions, of all possible configurations is studied:

- (a) ELS-1 with spin up (Fig. 2.11(a)).
- (b) ELS-2 with spin up (Fig. 2.11(b)).
- (c) ELS-1 with spin up and ELS-2 with spin up (Fig. 2.11(c)).
- (d) ELS-1 with spin up and ELS-2 with spin down (Fig. 2.11(d)).

Figure 2.10(b) shows, ΔE for these cases. The cases with one-ELS are degenerate while the energy differences for the case with two-ELSs show that there is some small interaction between them (point d is a bit higher in energy than point c). For closer ELSs we see that there is larger interaction between them, similar to the interaction between magnetic impurities through conduction electrons (RKKY interaction) [61, 62, 63]. The exact spatial dependence of the interactions and comparison to RKKY interaction is left for future studies.

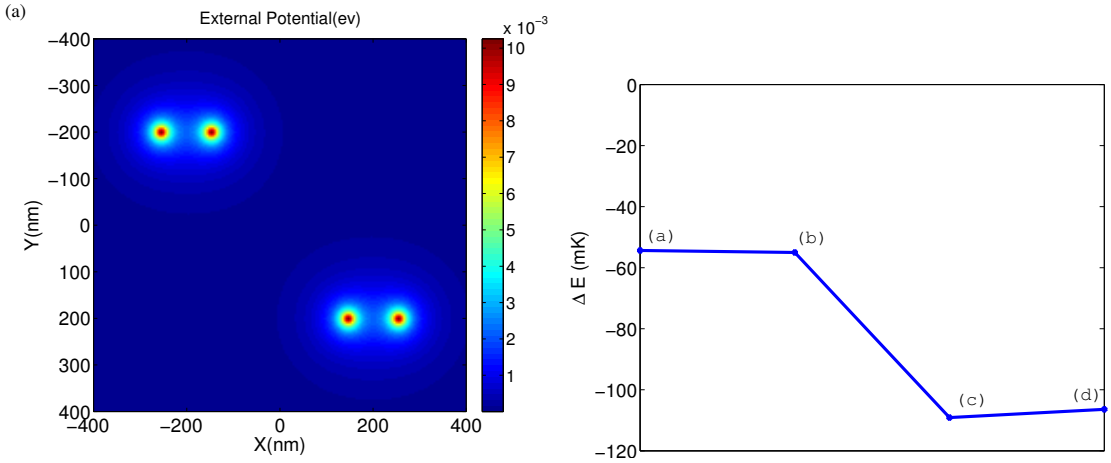

Figure 2.10: **(a)** Two saddle-point potential. **(b)** ΔE for different polarization configurations: (a) ELS-1 with spin up, (b) ELS-2 with spin up, (c) ELS-1 with spin up and ELS-2 with spin up, and (d) ELS-1 with spin up and ELS-2 with spin down.

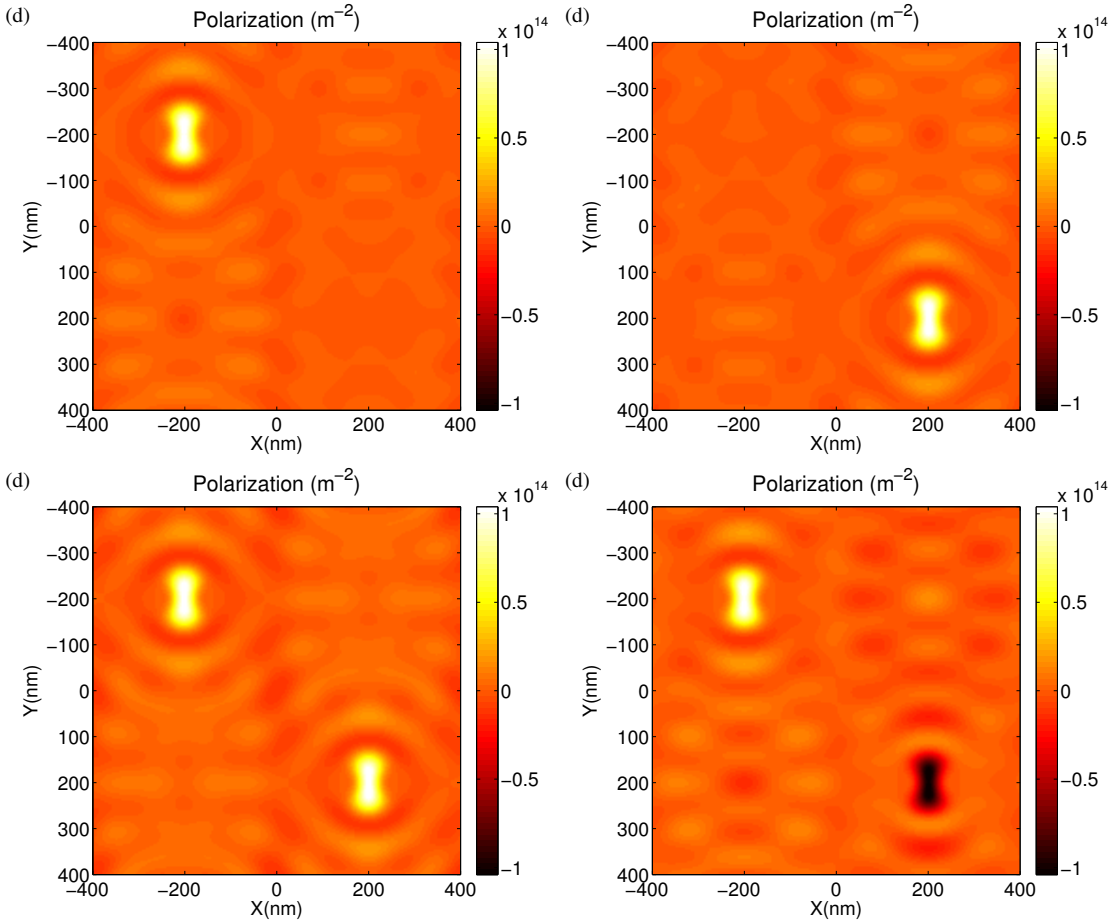

Figure 2.11: Two saddle-point polarization configurations: **(a)** ELS-1 with spin up, **(b)** ELS-2 with spin up, **(c)** ELS-1 with spin up and ELS-2 with spin up, and **(d)** ELS-1 with spin up and ELS-2 with spin down.

Having understood the properties of single and double ELSs, we can now create a random potential and study the possible polarized solutions as a function of the density. In this case we polarize the sample using a uniform magnetic field so that all the ELSs point in the same direction. Figure 2.12 shows such a random potential and the polarization for different electron densities. We can see that the ELSs form at various locations of the disorder potential and change their location as the density changes. At high densities, relative to the strength of the disorder potential, there is no longer a polarized solution.

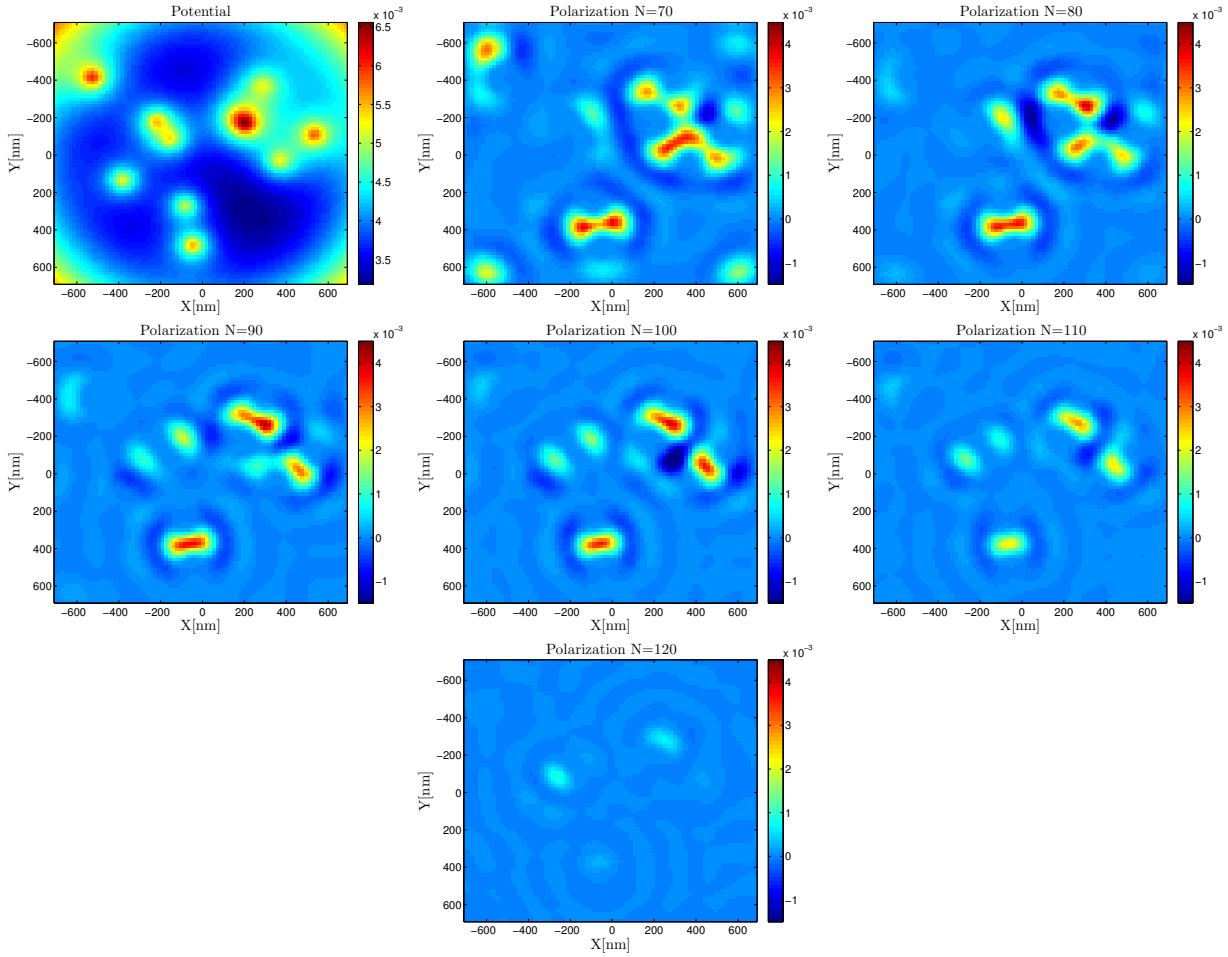

Figure 2.12: Random disorder potential, and the polarization for different densities. As the density increases the ELSs changes their location, until they disappear at high density (relative to the external potential strength).

2.4 Conclusions

The apparent saturation, or the deviation from the expected electron-electron interaction picture, of the coherence time at low temperatures is still a matter of debate. Our numerical SDFT simulation showed that Friedel oscillations can develop into a self-consistent localized state in an open two-dimensional systems. These states are formed at various saddle-points of the disorder potential (depending on the electron density at the bulk) at low temperatures, and can contribute to low-temperature dephasing through spin flip scattering above their corresponding Kondo temperatures. The distribution of the Kondo temperatures will determine the low temperature dependence of the dephasing rate. This involves more elaborate numerical calculation and will be left to future studies.

Chapter 3

Low Temperature Dephasing and the Quantized Hall Insulator

The quantum Hall transition [64] is one of the simplest and most studied quantum phase transitions. Nevertheless, the experimental observation of a new phase in this regime, the quantum Hall insulator, remains a puzzle since the first report more than a decade ago [32, 33, 34, 35, 36, 37, 38, 39]. This is because it contradicts all theoretical studies based on microscopically coherent quantum calculations [40, 41, 42, 43]. In this work, we introduce into the coherent quantum theory a new ingredient – incoherent events – in a controlled manner. Using direct numerical solutions, we demonstrate that these decoherence events stabilize the elusive quantum Hall insulator phase, which becomes even more stable with increasing temperatures and voltage bias, which is in agreement with experiments.

3.1 Integer Quantum Hall Effect

It is well known that under the influence of a magnetic field the transport properties of conductors change significantly. The application of a magnetic field perpendicular to the

direction of the current results in a potential drop along the transverse direction (V_1 and V_3 voltage probes shown in Fig.3.1), which is proportional to the magnetic field strength. In addition, the sign of the potential difference depends on the direction of the magnetic field. This voltage difference, termed the Hall voltage, give rise to the Hall (transverse) resistivity, $\rho_H = V_H/I$ where I is the total current that passes through a sample.

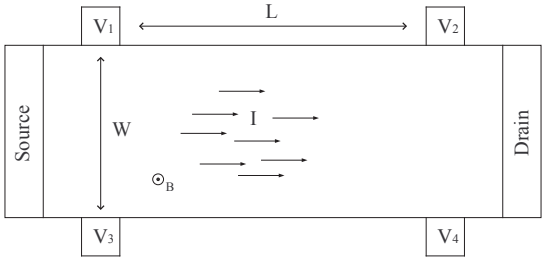

Figure 3.1: A scheme of Hall's measurement: The longitudinal voltage is measured between voltage probe V_1 and V_2, and the Hall voltage between V_1 and V_3.

The integer quantum Hall effect [64] has been a paradigm for two-dimensional quantum phase transitions: a transition between the quantum Hall phase, characterized by a quantized Hall resistance ρ_{xy} and a vanishing longitudinal resistance ρ_{xx} , and an insulator, characterized by diverging ρ_{xx} and ρ_{xy} (see Fig.3.2).

For a clean two-dimensional system under a perpendicular magnetic field, the eigenstates are the Landau levels (LL), and the eigenenergies are given by

$$E_N = (n + \frac{1}{2})\hbar\omega_c, \tag{3.1}$$

where $\omega_c = |e|\, B/m_e$ and n is the LL number. An important parameter is the filling factor ν, which is the ratio between the number of electrons to the number of flux quanta $\Phi_0 = h/e$ that penetrate the sample. Since the spatial spread of the eigenstates of the electron are of the order of the magnetic length $l_c = \sqrt{\hbar/\,|e|\, B}$, we can see that the flux that penetrates each electron "territory" is exactly one flux quantum, so that the filling factor also gives the

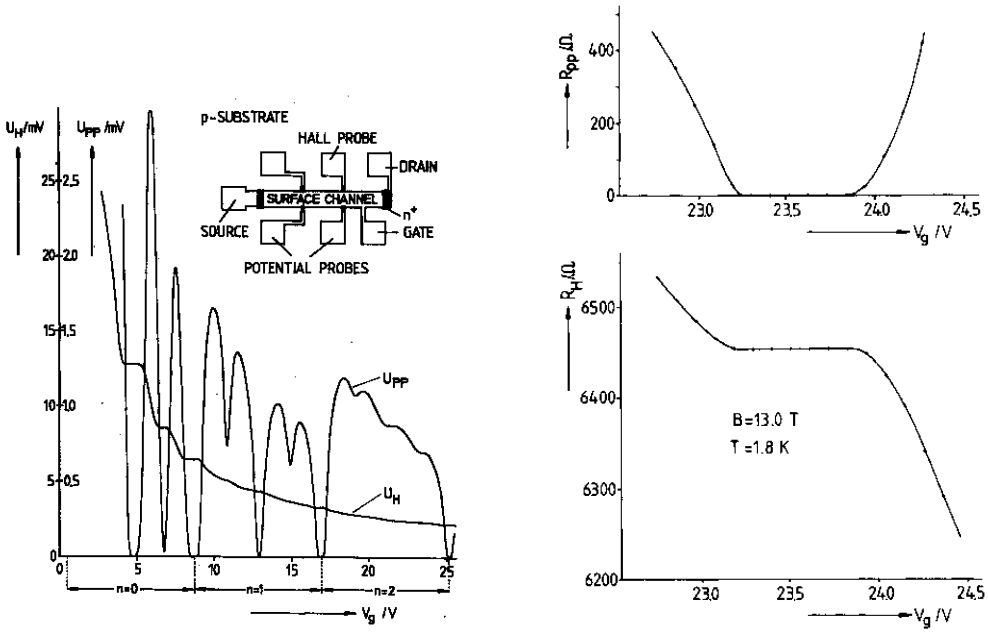

Figure 3.2: **Left:** measurement of the Hall voltage U_H, and the longitudinal voltage drop U_{pp} as a function of the gate voltage V_g at $T = 1.5K$. The magnetic field is $B = 18T$ and the source drain current is $1\mu A$. The inset shows a top view of the device. **Right:** Hall resistance R_H, and longitudinal resistance R_{pp}. Figures taken from [64].

number of filled LLs

$$\nu = \frac{N\Phi_0}{BS} = \frac{n_e\Phi_0}{B}, \tag{3.2}$$

where N is the number of electrons, n_e their density, and S is the area of the sample. In the experiment, the filling factor can be altered by a change in the magnetic field B or in the electron density n_e.

To understand the role of electron localization, let us look at the semi-classical limit, which is valid in the limits of a strong magnetic field, where the magnetic length, which basically determines the electron wavelength, is much smaller than the typical length scale of the disorder potential. In the presence of disorder (realized, e.g., by impurities in the lattice), the electrons are localized along equipotential contours of the potential. For a random

potential with zero average, when the Fermi energy is at the center of the LL energy (due to the disorder, the LLs are broadened), the electron states become extended and can percolate through the system, giving rise to a finite longitudinal resistance and a change in Hall resistance. Thus, when the energy is scanned, each time the Fermi energy passes through the center of an LL, the extended states contribute to the Hall conductance σ_{xy} a single conductance quanta e^2/h. In between the LL, all the states are localized and do not change Hall conductivity so that,

$$\sigma_{xy} = \frac{e^2}{h} \times n, \tag{3.3}$$

where n is the number of filled LLs. This semi-classical model explains both the plateaus in Hall conductivity and the vanishing of longitudinal conductivity in terms of localized and delocalized states. We should also note that when the filling factor is smaller than one (for a large magnetic field, for example), there are no single-particle extended states in the system and the non-interacting system behaves as an insulator where both ρ_{xx} and ρ_{xy} diverge.

3.2 Quantized Hall Insulator

As explained in the previous section, the QH system has only two phases: the insulating phase where both ρ_{xx} and ρ_{xy} diverge, and the QH phase where $\rho_{xx} = 0$ and ρ_{xy} is quantized. However, as discussed below, measurements have shown that under very strong magnetic fields and at low temperatures the system exhibits a new phase, characterized by $\rho_{xx} \to \infty$, while ρ_{xy} stays quantized to its value at the last plateau of the QH phase. In this section, we will review the experimental evidence and a few theoretical studies regarding this new phase (for a comprehensive review, see [65]).

3.2.1 Experimental Evidence

In an experimental study done by Shahar *et al* [32], the longitudinal and Hall resistivities were measured in a 2d hole system for a wide range of magnetic fields (B) and at low temperatures (as low as 0.3K). An inspection of longitudinal resistivity as a function of temperature reveals two critical magnetic fields. In those critical magnetic fields, longitudinal resistivity is temperature-independent, as shown in Fig. 3.3. Between these two critical magnetic fields, there is the regular QH phase, which is characterized by a quantized Hall resistivity and a ρ_{xx} that decreases toward zero as the temperature goes down. In the higher field, the dependence of ρ_{xx} on temperature is inverted and increases exponentially as the temperature decreases, indicating an insulating behavior. This divergence of ρ_{xx} hinders the determination of ρ_{xy} due to Hall contact misalignment, which causes mixing between the measured ρ_{xx} and ρ_{xy}. That problem is dealt with through the anti-symmetrizing of the measurement, which is achieved by measuring in an opposite magnetic field as well, and a taking of the antisymmetric part in B, as shown in the inset of Fig. 3.3. Strikingly, Hall resistivity at a high B field, $B > B_c$, stays almost quantized to the value h/e^2 over a wide range of B extending up to $4T$ from the critical field B_c (shown in Fig. 3.3). That measurement was not unique; this kind of behavior has also been demonstrated in subsequent experiments [33, 34, 35, 36, 37, 38, 39] and under higher magnetic fields.

This phase, coined the quantized Hall insulator (QHI), cannot be explained by the standard theory that describes the QH phase. At the moment there is no complete theory that explains this new phase.

3.2.2 Theoretical Models

The first work that suggested a unique behavior in a strong magnetic field limit was published by Kivelson, Lee and Zhang [66]. Basing themselves on a set of laws of corresponding states, they predicted that, in the insulating phase $\rho_{xy} \sim B/nec$, while $\rho_{xx} \to \infty$ as the temperature

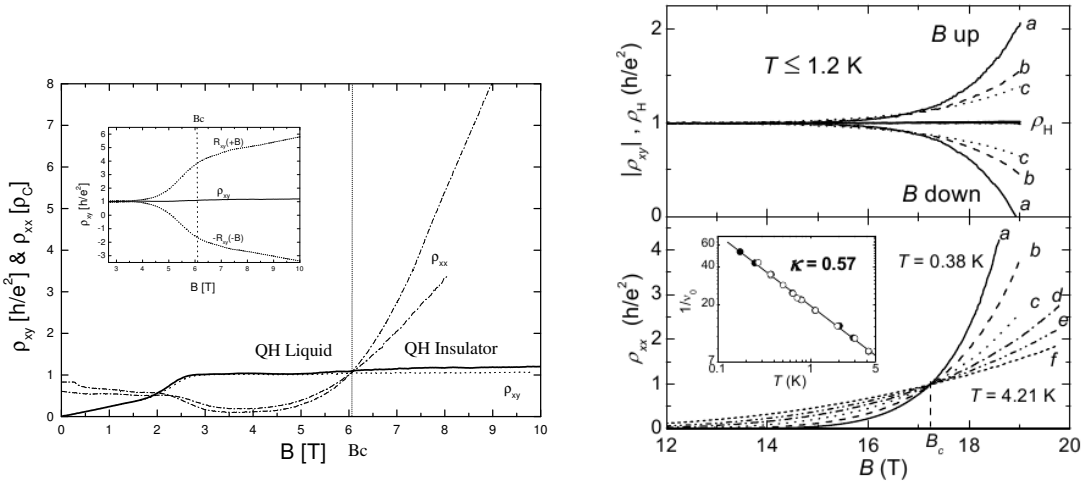

Figure 3.3: The Hall and diagonal resistivity as a function of magnetic field. **Left:** The solid line is Hall resistivity measured at T=300 mK and a current of I=200 nA, where the dotted line represents I=400 nA. The dash-dotted lines are ρ_{xx} at T=1.2 K (the uppermost curve) and at T=4.2 K (the lower curve). V_G=5.2 V, $\rho_c = 1.65h/e^2$ and B_C=6.06 T. The inset shows Hall resistances for $+B$ and $-B$ in dotted lines and the anti-symmetric part of ρ_{xy} is represented by a solid line, from [34]. **Right:** Longitudinal (lower frame) and Hall resistivity (upper frame). Hall resistivity obtained by an averaging of both field polarities is quantized at h/e^2 for $T \leq 1.2K$. The letters a,b,....f indicate T = 0.38, 0.65, 1.2, 2.1, 2.9 and 4.2 K. Taken from [37]

drops to zero (they named this phase the Hall insulator). Note, however, that this phase is a *classical* Hall insulator; in other words, Hall resistance is not expected to be quantized, which is in disagreement with the-above mentioned experimental observations.

Using a renormalization group approach, Pruisken [67] calculated the flow of the magneto-conductance tensor shown in Fig.3.4. From this flow diagram, we can see that there are fixed points for $\sigma_{xx} = 0$ and $\sigma_{xy} = \frac{e^2}{h}n$. When n equals zero, we are again in the insulating phase, in which both longitudinal and Hall resistivity diverge. When, n equals to an integer, the system is in the QH plateau phase.

Entin-Wohlman *et al.* [40] investigated the transport properties of an electron in a phonon-assisted hopping regime, that included coherent effects. In order to include the contribution of the magnetic flux, a triangular cluster with three sites (each representing a wave function

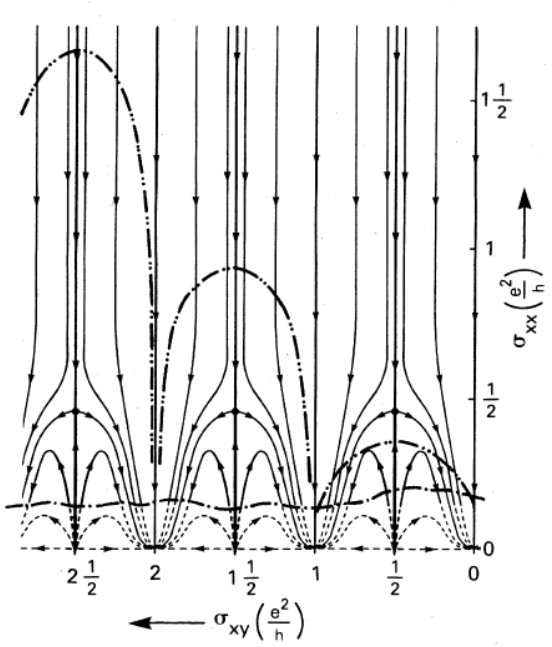

Figure 3.4: The RG flow diagram as obtained from the dilute instanton gas method. Figure taken from [67].

localized at that site) was introduced. Transport from site 1 to site 2 involved interference between the direct path from site 1 to site 2 and the indirect path through site 3 ($1 \to 3 \to 2$), depending on the magnetic flux that penetrates the triangle. These researchers were thus able to obtain the distribution of the conductivity tensor. Their calculation shows that the results depend on whether one averages the conductivity or the resistivity and also on whether the experiment is a DC or AC. They argue that, for an AC measurement, the appropriate averaging procedure is to average the conductivity tensor, while the averaging of the resistivity tensor is equivalent to a DC measurement. Thus, by using an averaging procedure that is equivalent to an AC measurement, one can obtain the Hall insulator phase (still with an arbitrary value of Hall resistance). However, when the averaging procedure is used to receive a DC measurement, both ρ_{xx} and ρ_{xy} diverge as the temperature decreases, with the relation $\rho_{xy} \sim \rho_{xx}^2$. Using an RG procedure, Zulicke and Shimshoni [42], confirmed

that both ρ_{xx} and ρ_{xy} diverge in the insulating regime. They also found that $\rho_{xy} \sim \rho_{xx}^{x}$ deep into the insulating phase, though with a different exponent ($x \sim 1/2$).

These studies were confirmed by Pryadko and Auerbach [41], who solved a four-lead finite Chalker-Coddington (CC) [30] network in a system of different sizes. In this network (shown in Fig. 3.5), each tunneling junction between the puddles (the puddles are defined as regions encircled by current-carrying channels, i.e., regions enclosed by equipotential contours) is represented by an unitary scattering matrix which is a matrix, connecting the two incoming and two outgoing channels (see Fig. 3.5b). Pryadko and Auerbach then went on to examine what happens in a system with a finite phase length by arguing that the dephasing length determines the finite size of the coherent system. Thus, the solution for different system sizes is equivalent to different dephasing lengths[1]. Their results, presented in Fig.3.6, show that again ρ_{xy} diverges exponentially, with increasing the phase coherence length.

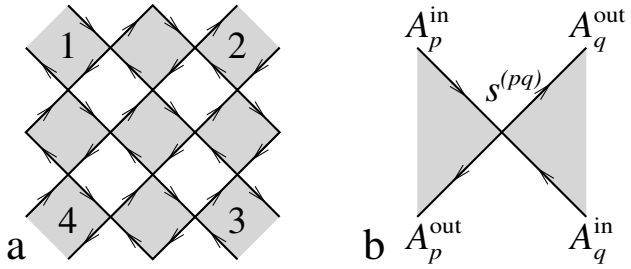

Figure 3.5: (a) Four-terminal $L = 6$ CC network. QH puddles are shaded. Edge currents with amplitudes A_p^{α} propagate along the arrows. (b) The incoming and outgoing amplitudes at the tunnel junction between puddles p and q are related by the scattering matrix. Figure taken from [41]

Concentrating on the limit of $L >> L_\phi \to 0$, Shimshoni and Auerbach [68] investigated a system in which the phase length is much smaller than the localization length. Their model is a network of puddles of QH Phase in constant densities, i.e., the Hall conductance of each

[1]That allows one to empirically include dephasing in the system, though the intermediate regime, where the system size and the dephasing length are of the same order, cannot be approached by this ad hoc argument.

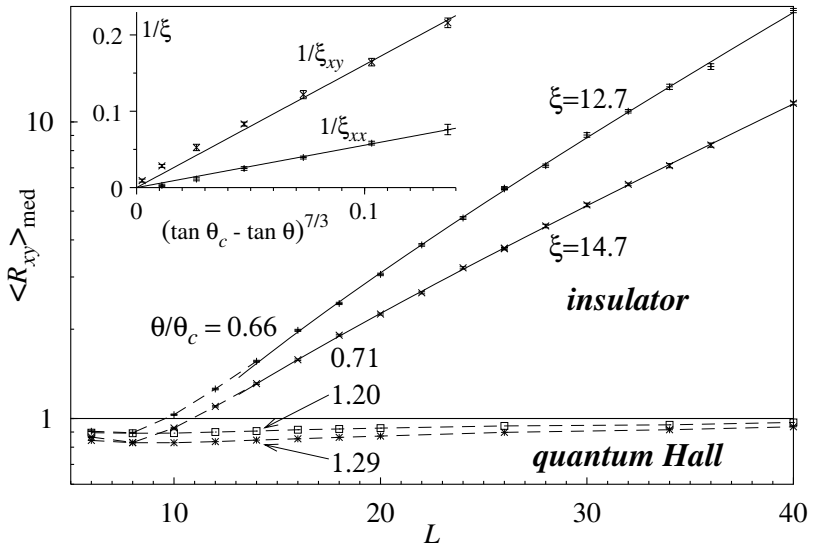

Figure 3.6: QH to insulator transition in finite size scaling. Inset: The resulting inverse correlation lengths are consistent with the critical exponent $\nu = 7/3$. Figure taken from [41]

puddle is quantized to the same value (see Fig. 3.7 where each puddle, has a single edge state). They assumed that there is no coherence between different puddles, and therefore the puddle network properties can be given by classical Kirchoff laws. As opposed to the prior models, this study suggests a robust quantization of ρ_{xy}. Since each puddle is in a QH phase, its Hall resistivity is quantized to h/e^2. Moreover, when connecting these puddles classically, as shown in Fig. 3.7 the effective Hall resistivity does not change but remains quantized. However, this model cannot account for the case of a large system with finite phase lengths ($L >> L\phi$) which is the relevant physical regime.

3.3 Incoherent Scattering

We may conclude from all the theoretical works presented here is that in a coherent regime interference effects localize the electrons and destroy the QHI phase. On the other hand, when the coherent length is much shorter than the localization length, the system exhibits a

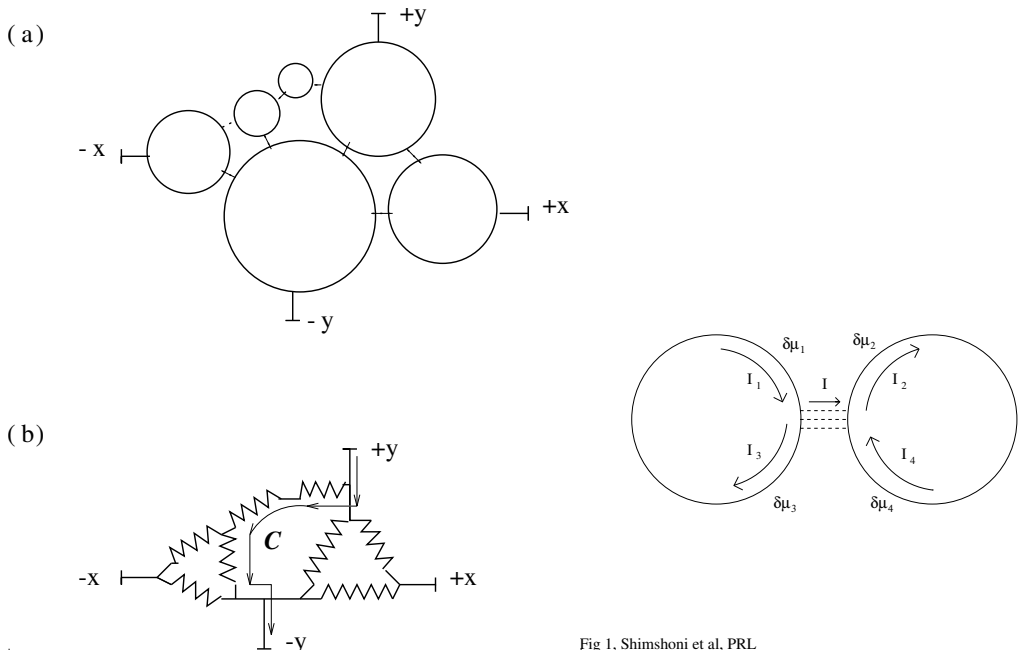

Figure 3.7: Left side:(a) Typical puddle network, where dotted lines represent constrictions. (b) Corresponding equivalent circuit. Right side: Single junction between puddles. Figure taken from [68]

robust quantization of Hall resistivity. In this work we will study the full crossover between these two extreme regimes, so that we can observe the behavior of the resistivity tensor as the system length becomes larger than the phase length. To do so one has to introduce dephasing into the system using a first-principle approach.

Büttiker's Approach to Dephasing

In order to introduce dephasing in these network models in a controlled manner so that the full crossover between quantum behavior to classical behavior can be realized, we used Büttiker's approach to dephasing [31]. The principal idea is to place between two elastic barriers a phase-randomizing scatterer, that destroys the interference effects that occur between the barriers. This phase-randomizing is realized by a coupling of the system to a reservoir via current-conserving contacts, which guarantees that, for every electron that enters

a reservoir, there is an electron that leaves it. However, the phase of the outgoing electron has no correlation with the phase of the incoming electron, so that interference effects are destroyed. The full crossover is reached by assigning each electron a finite probability to enter the reservoir. When this probability is zero, the system is fully coherent. When it is unity, the system is classical, with no coherent transport. Tuning this probability from zero to unity allows us to probe the crossover between fully coherent to fully incoherent regimes.

3.4 Model and Results

In order to incorporate Büttiker's method for dephasing with the CC model of 2d network (for a full derivation of the general case, see appendix B), we used a scheme of the random potential as shown in Fig.3.8a. The black lines represent equipotential lines and the wiggly lines represent incoherent events. Since the incoherent events do not backscatter the chiraly moving electrons, we coupled each channel in the model (i.e., forward and backward propagation) to separate current-conserving reservoirs. In Fig.3.8b we show our basic unit and the way the coupling to the reservoirs is done. We also add a scattering matrix before each reservoir to allow us to control the rate of the dephasing through its transmission amplitude ϵ. When $\epsilon = 0$, the reservoirs are uncoupled and the transmissions and reflections are coherent; when $\epsilon = 1$, every electron enters into the reservoirs and the behavior is totally incoherent. Scattering between different equipotential contours happens only at the saddle points of the potential, which is represented by additional scattering matrices with transmission amplitudes that control the scattering between the different puddles. These transmission amplitudes depend on the strength of the magnetic field and on the height of the potential barrier, as was shown by Fertig and Halperin [69]:

$$\begin{aligned} \mathcal{T} &= \frac{1}{1+\exp(-\pi z)}, \\ z &= \frac{E-V_0}{l_c^2 (U_x U_y)^{1/2}}, \end{aligned} \tag{3.4}$$

where E is the energy of the electron, V_0 is the height of the saddle point, U_x, U_y are the second derivatives of the potential, and $l_c = \sqrt{\hbar/|e|B}$ is the magnetic length; thus z can be regarded as the dimensionless height of the saddle point. Close to the percolation threshold $E \approx V_0$, we can expand the transmission and obtain the relation $\mathcal{T} \propto 1/B \propto \nu$.

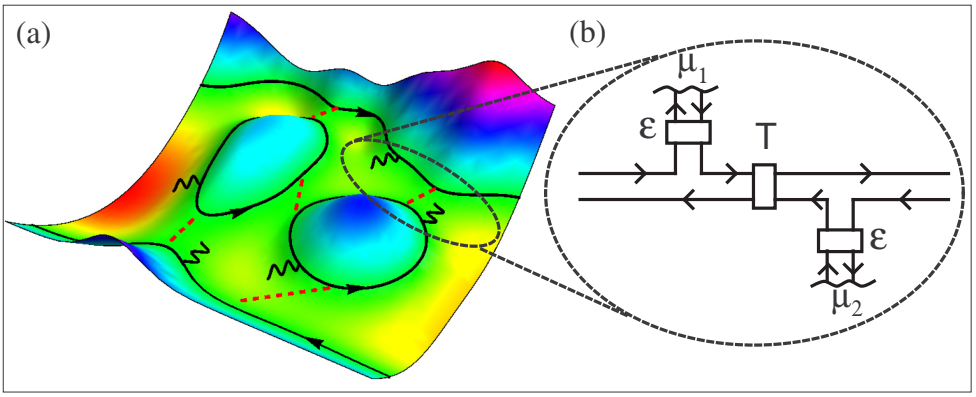

Figure 3.8: Schematic description of the model: **(a)** The potential landscape. In a strong magnetic field, electrons follow equipotential lines (thick lines) and may undergo incoherent scattering events (wiggly lines). Near saddle points an electron can tunnel from one equipotential line to another, with a corresponding scattering matrix. Such a junction, including the possibility of quantum tunneling and of incoherent scattering, is represented by the elementary unit **(b)**, characterized by transmission probability $\mathcal{T}$ and dephasing parameter ϵ.

Each scatterer in the CC network is depicted as a blue dot in figure 3.9 and is replaced by this basic unit cell. The result is a network with controlled dephasing. Tuning this probability ϵ from zero to unity allows us to probe the crossover between fully coherent to fully incoherent regimes.

We first solve numerically for ρ_{xx} and ρ_{xy} for a network of size $L \times L$ (Fig. 3.9), for different

values of the average transmission though a saddle point $\mathcal{T}$, and decoherence parameter ϵ. $\rho_{xx} \equiv (1-T)/T$ is determined by the effective transmission T through the whole system. As in the experiment, ρ_{xy} is determined by V_H, the anti-symmetric component of the difference between the chemical potentials (Eq.B.10 in appendix B) at the upper and lower branches of the structure with respect to the magnetic field, which is nonzero due to the chiral nature of the problem: $\rho_{xy} \equiv V_H/I$, where I is the current. Since both ρ_{xx} and ρ_{xy} are exponentially distributed, we have used a logarithmic average [42] to calculate the effective renormalized values. The values of the saddle-point transmission probabilities $\mathcal{T}$ are taken from a wide distribution, with a predefined average, while the coupling to the current-conserving reservoirs ϵ is taken from a delta distribution.

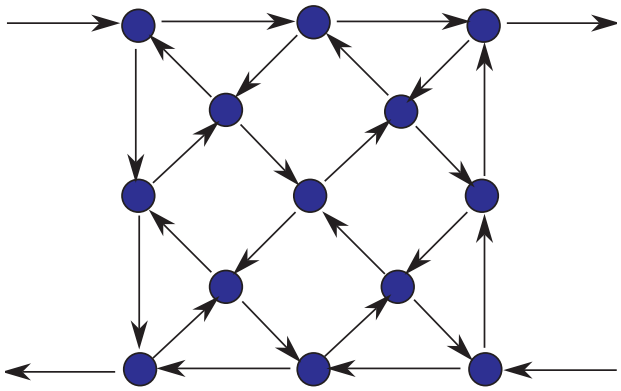

Figure 3.9: CC network of size 3×3; each blue dot represents a basic unit cell with one scatterer and two current-conserving reservoirs with entering probability ϵ.

In Fig. 3.10, we plot ρ_{xx} (a) and ρ_{xy} (b) as a function of the size of the system, for different values of the dephasing parameter ϵ. In the insulating phase ($\mathcal{T} < \mathcal{T}_c$), and in the absence of decoherence events ($\epsilon \to 0$), consistent with previous studies [41] both ρ_{xx} and ρ_{xy} increase exponentially. In the presence of decoherence, ρ_{xx} first increases with system size (for $L < L_\phi$), and then saturates, as one would expect in a classical system. Surprisingly, while ρ_{xy} also initially increases, for $L < L_\phi$, it reaches a maximum and then decreases. For samples with larger ϵ (smaller L_ϕ), ρ_{xy} decreases all the way to unity (all resistance values are expressed

in units of h/e^2, where h is the Planck constant and e the electron charge). Although, for samples with smaller ϵ, ρ_{xy} does not reach the asymptotic regime, $L \gg L_\phi$, we demonstrate, in Fig. 3.10c, that all the curves collapse when plotted as $\rho_{xy} - 1$ vs L. This indeed confirms that, independent of ϵ (or L_ϕ), ρ_{xy} scales as $\rho_{xy} = 1 + c_\epsilon f\,(L/L_\phi)$, with $f(x) \sim 1/\sqrt{x}$ for large x. This phase, where ρ_{xy} is quantized to unity and ρ_{xx} could be exponentially large, is the elusive quantum Hall insulator phase.

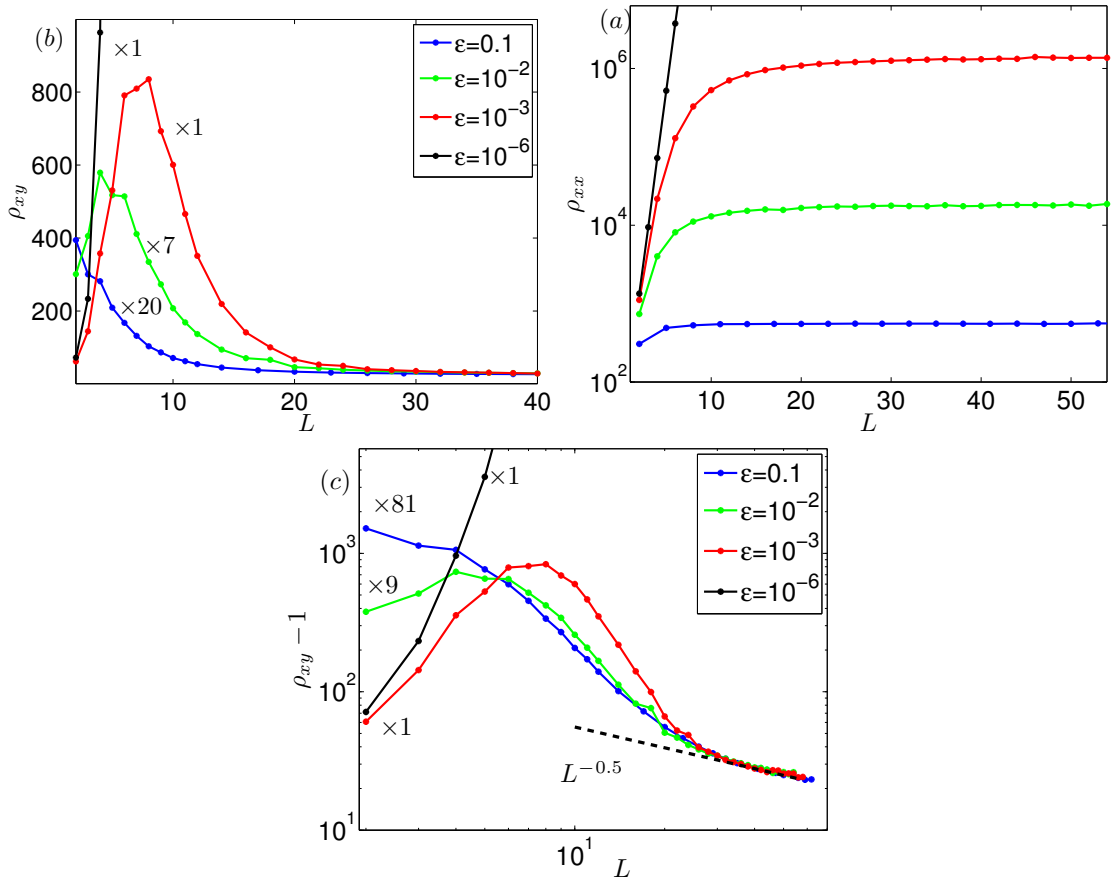

Figure 3.10: ρ_{xx} **(a)** and ρ_{xy} **(b)** from the network model as a function of network size for several values of the dephasing parameter ϵ (values depicted in (b)), and average transmission of a single scatterer $< \mathcal{T} >= 0.13$. While ρ_{xx} saturates at $L \gg L_\phi$, ρ_{xy} exhibits a nonmonotonic behavior. **(c)** Same data as in (b), plotted as $\rho_{xy} - 1$, multiplied by a constant, as a function of size on a double-log scale. At large sizes, all curves collapse onto a single curve, confirming that, for large sizes, $\rho_{xy} \to 1$.

While the decrease of ρ_{xy} towards unity, as the system size increases, seems surprising a priori, one can show that it is a direct consequence of the rules of connecting resistors in series and in parallel. To demonstrate this point, we have calculated R_{xx} and R_{xy} (the longitudinal and Hall resistances for non-square systems) for a stack of coherent ordered squares, each of size $L_0 \times L_0$, where the only decoherence scatterers are at the corners of these elementary squares (see inset of Fig. 3.11), connected either in series (Fig. 3.11a) or in parallel (Fig. 3.11b). For the series connection, we find that as expected R_{xx} increases linearly with system length L and R_{xy} saturates, while, for the parallel connection, both R_{xx} and R_{xy} decrease as $1/W$, where W is the width of the sample, with the former toward zero, again as expected, and the latter toward unity. This same behavior is also observed for rectangular disordered network-model systems (not shown). Both these behaviors of R_{xy} can be readily understood as follows. We note that since $I = TV$, where V is the voltage difference between source and drain, and $R_{xx} = (1 - T)/T$, one can write $R_{xy} = (V_H/V)(R_{xx} + 1)$. For the series connection, when $L \gg L_\phi$, one can think of the system as consisting of L/L_ϕ coherent segments, connected incoherently. Thus, the voltage drop in each segment is VL_ϕ/L. Since the Hall voltage of each segment is linearly dependent on the voltage drop across that segment, it scales like $1/L$, and, as R_{xx} grows linearly with L, R_{xy} remains constant. On the other hand, as the system width W increases, for constant length, R_{xx} decreases as $1/W$, and, thus, the above relation dictates that R_{xy} also decreases (because V_H is bound from above by V).

In fact, in this limit, the upper chemical potential becomes dominated by the source chemical potential, while the lower chemical potential becomes dominated by the drain chemical potential. Thus V_H/V approaches unity as the width increases. Consequently, as R_{xx} approaches zero with increasing width, R_{xy} approaches unity. (This is in contrast with the analysis of Ref. [41], which claims that R_{xy} remains constant as the width increases, while R_{xx} decreases toward zero, violating the above relation between R_{xx} and R_{xy}.) Thus, ρ_{xy} for a large square of size $L \times L$ can be obtained by first making the system longer, of length L, such that its R_{xy} stops changing, and then increasing its width to L, so that Hall resistance

decreases toward unity. This observation is also consistent with the two-phase approach [70].

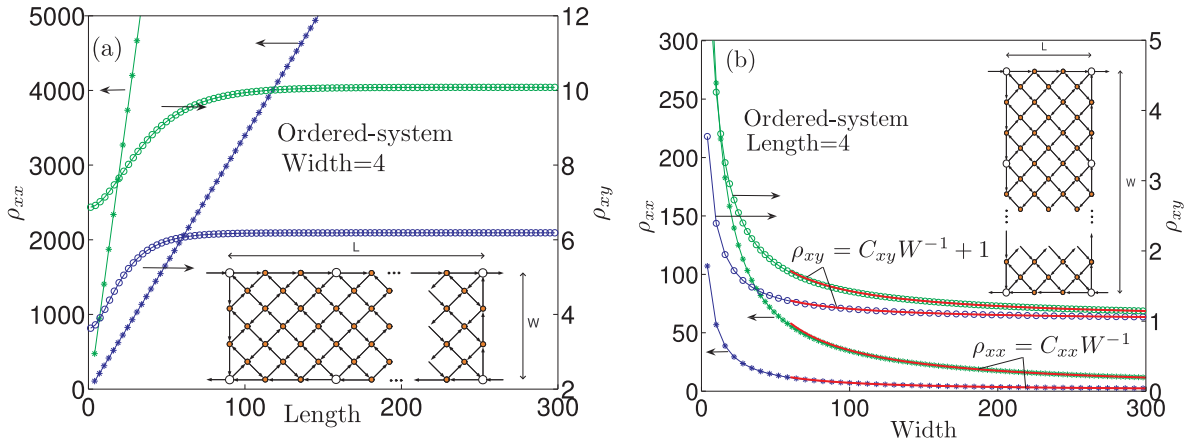

Figure 3.11: **(a)** ρ_{xy} and ρ_{xx} for ordered system (same phase and transmission value for all the scatterers) as a function of length for system of fixed width $W = 4$; the green color is for $\mathcal{T} = 0.05$ and the blue is for $\mathcal{T} = 0.1$. Here dephasing occurs only at the corners of the elementary squares (4×4 networks, plotted as empty dots) for which $\epsilon = 1$. ρ_{xx} grows linearly with the length while ρ_{xy} saturates. **(b)** For a system of fixed length, as the system becomes wider, ρ_{xy} goes to unity (C_{xy} equals 43 and 17.6 for $\mathcal{T} = 0.05$ and $\mathcal{T} = 0.1$ respectively). ρ_{xx} goes to zero as expected, with C_{xx} equaling 3500 and 718 for $\mathcal{T} = 0.05$ and $\mathcal{T} = 0.1$ respectively.

We also compare our results in Fig. 3.12 to the experimental data. Panels (a) depict our calculation and the experimental data [32] (inset of (a)). ρ_{xx} and ρ_{xy} are plotted as a function of the distance from the critical point ($\mathcal{T} - \mathcal{T}_c$ in the theoretical curves, $B - B_c$ in the experimental curve). Several theoretical curves, for a system of fixed L, but of different ϵ (or L_ϕ), are plotted, demonstrating that the quantization of ρ_{xy} in the quantum Hall insulator phase becomes more exact as the level of decoherence increases (larger ϵ, smaller L_ϕ). Interestingly, the experimental curves exhibit better quantization with increasing temperature, which we attribute to increased decoherence.

Enhanced decoherence also explains the better quantization of ρ_{xy} for higher currents [34]. For even higher temperatures, approaching the energy gap in the quantum Hall regime,

one observes a breakdown of the quantization in both phases – in the quantum Hall phase and in the quantum Hall insulator phase [34, 35, 36, 39]. Another striking feature of the experimental data [32] was the symmetry of ρ_{xx} on the two sides of the critical point, $\rho_{xx}(\Delta\nu) = 1/\rho_{xx}(-\Delta\nu)$, where ν is the filling factor, the number of electrons in the system per available states in a Landau level (inset of Fig. 3.12b). This symmetry is also manifested in our results (Fig. 3.12b). In the coherent case, it can be traced to the symmetry of the disorder potential, which leads to $\mathcal{T}_c = 1 - \mathcal{T}_c = 1/2$. In that case, it is easy to see [43] that since, by definition, in the fully coherent case $\rho_{xx}(\mathcal{T}) = \mathcal{T}/(1-\mathcal{T})$, then clearly $\rho_{xx}(\mathcal{T}_c + \Delta\mathcal{T}) = (\mathcal{T}_c + \Delta\mathcal{T})/(1 - \mathcal{T}_c - \Delta\mathcal{T}) = 1/\rho_{xx}(\mathcal{T}_c - \Delta\mathcal{T})$. In the presence of incoherent scattering, ρ_{xx} is given, as discussed above, by the coherent ρ_{xx} on a scale of L_ϕ. The experimental deviations from this symmetry (inset of Fig. 3.12b) thus make it possible to investigate the dependence of the decoherence length on the magnetic field and density, providing a deeper understanding of the nature of incoherent processes at such low temperatures.

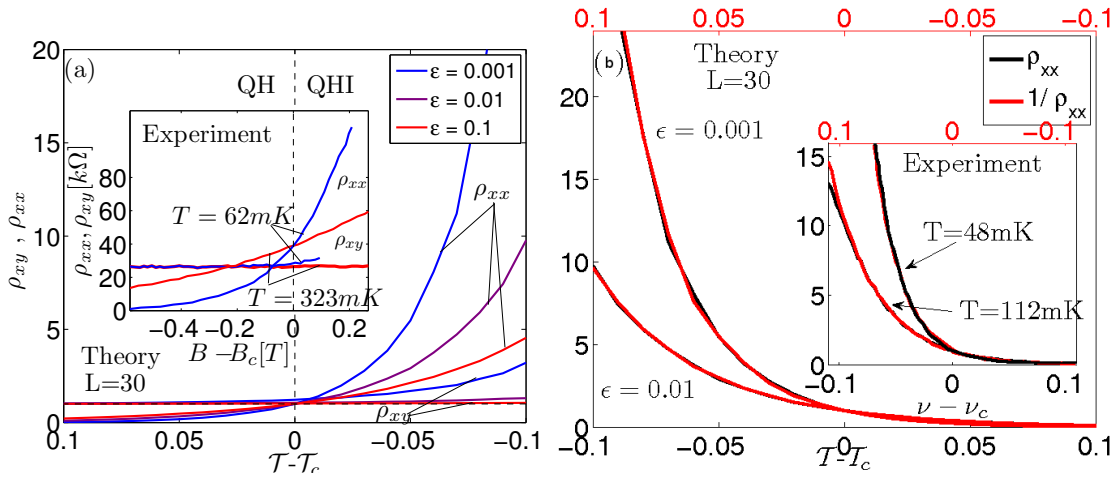

Figure 3.12: Theoretical **(a)** and experimental [32] (inset of **(a)**) results for longitudinal and Hall resistivity plotted as a function of the deviation from the critical point for systems with different phase lengths (theory) or temperatures (experiments). The quantization of Hall resistance on the insulating side improves with increasing decoherence (theory) or temperature (experiment). Symmetry between the quantum Hall phase and the insulating phase. ρ_{xx} on the insulating side and $1/\rho_{xx}$ on the quantum Hall side, experiment [32] (inset of **(b)**) and theory **(b)**. Theoretical results are for a system with finite phase length. The data is plotted with the axis for $1/\rho_{xx}$ inverted (top axis), for two different temperatures (experiment) and phase lengths (theory), demonstrating the symmetry between the two phases. The inset demonstrates that this symmetry is obeyed in the theory for many orders of magnitude.

3.5 Conclusion

The existence of incoherent scattering at milli-kelvin temperatures, imperative, as shown here, for explaining the quantum Hall insulator phase, is also supported by the fact that ρ_{xx} is still temperature-dependent, indicating that the system size is larger than L_ϕ. Incoherent scattering should be explored in the context of other quantum phase transitions as well. In particular, it may also explain other puzzling two-dimensional phenomena, such as the apparent metal-insulator transition [71, 72] or the intermediate metallic phases observed in the superconductor-insulator transition in disordered thin films [73] and in the quantum Hall to insulator transition [74]. The present calculation allows quantitative determination of the incoherence length, which is important for any possible application of mesoscopic devices.

Conclusion

In this work we dealt with several aspects of many-body interactions in the field of mesoscopic physics. We started with an SDFT model of a length tunable QPC. We showed that Friedel oscillations generically develop into ELSs whose number grows with the QPC length, leading to alternating parity in the ELS that is consistent with a periodic modulation between single-peak and double-peak ZBAs that observed in the experiment. We showed that the periodic character of both the ZBA and the 0.7 anomaly as a function of QPC length provides evidence that the physics of Friedel oscillations is fundamental to these phenomena. Next we showed that these localized states can also form in an open two-dimensional system at the saddle points of the disorder potential. These states can contribute to low-temperature dephasing through spin flip scattering above their corresponding Kondo temperature and may explain the apparent saturation in coherence time observed in experiments. Last, using the semi-classical model of a CC network with current conserving reservoirs we considered the effect of incoherent scattering under a strong magnetic field, where we were able to control the coherence length of the system. We showed that when taking into account incoherent scattering the quantum Hall insulator phase becomes a stable phase.

Appendix A

Spin Density Functional Theory

Kohn-Sham spin-density functional theory [75] is one of the most widely used methods of electronic structure calculation in condensed-matter physics, owing to its simplicity and relatively low computational complexity. The main idea is to replace the many-body Schrödinger equation by a one-electron Schrödinger equation with an effective potential that is a functional of the electron density,

$$(\frac{1}{2}\nabla^2 + v(\mathbf{r}) + u([n];\mathbf{r}) + v_{xc}^{\sigma}([n_\uparrow, n_\downarrow];\mathbf{r}))\psi_{\alpha\sigma}(\mathbf{r}) = \epsilon_{\alpha\sigma}\psi_{\alpha\sigma}(\mathbf{r}), \tag{A.1}$$

$$n_\sigma(\mathbf{r}) = \sum_\alpha f(\mu - \epsilon_{\alpha\sigma}) \left|\psi_{\alpha\sigma}(\mathbf{r})\right|^2, \tag{A.2}$$

where the σ is spin index and α stands for the set of remaining quantum numbers. $f(\mu - \epsilon_{\alpha\sigma})$ is the Fermi distribution function. The effective potential includes a classical Hartree potential

$$u([n];\mathbf{r}) = \int d^3r' \frac{n(r')}{|r - r'|}, \tag{A.3}$$

and v_{xc}^{σ} is the exchange-correlation potential. In principle, this method is exact for the calculation of the spin-density of the ground state but only an approximation for v_{xc}^{σ} is available. Given the best approximate in two-dimensions [48], Equations A.1 and A.2, are solved self-consistently until the energy converges.

A.1 Hohenberg Kohn Theorems

Following Hohenberg and Kohn [76], we consider a collection of an arbitrary number of spinless interacting electrons in a large box under the influence of an external potential $v(\mathbf{r})$. The Hamiltonian has the form

$$H = T + V + U \tag{A.4}$$

where

$$T = \frac{1}{2}\int \nabla\psi^{\dagger}(\mathbf{r})\nabla\psi(\mathbf{r})d\mathbf{r}, \tag{A.5}$$

$$V = \int v(\mathbf{r})\psi^{\dagger}(\mathbf{r})\psi(\mathbf{r})d\mathbf{r}, \tag{A.6}$$

$$U = \frac{1}{2}\int \frac{1}{|\mathbf{r}-\mathbf{r}'|}\psi^{\dagger}(\mathbf{r})\psi^{\dagger}(\mathbf{r}')\psi(\mathbf{r}')\psi(\mathbf{r})d\mathbf{r}d\mathbf{r}'. \tag{A.7}$$

For simplicity we deal only with a nondegenerate ground state. The electronic density in the ground state Ψ is:

$$n(\mathbf{r}) = \left\langle \Psi|\psi^{\dagger}(\mathbf{r})\psi(\mathbf{r})|\Psi\right\rangle, \tag{A.8}$$

which is a functional of the external potential. In order to show that $v(\mathbf{r})$ is a functional of $n(\mathbf{r})$, we use *reductio ad absurdum*. Let us assume that another potential $v'(\mathbf{r})$ that satisfies $v(\mathbf{r}) - v'(\mathbf{r}) \neq const$, with ground state Ψ' gives rise to the same density $n(\mathbf{r})$. The ground state energy will then satisfy

$$E' = \langle\Psi'|H'|\Psi'\rangle < \langle\Psi|H'|\Psi\rangle = \langle\Psi|H + V' - V|\Psi\rangle, \tag{A.9}$$

so that

$$E' < E + \int (v'(\mathbf{r}) - v(\mathbf{r}))n(\mathbf{r})d\mathbf{r}. \tag{A.10}$$

Interchanging the primed and unprimed, we obtain

$$E < E' + \int (v(\mathbf{r}) - v'(\mathbf{r}))n(\mathbf{r})d\mathbf{r}. \tag{A.11}$$

Addition of A.10 and A.11 gives:

$$E + E' < E' + E \tag{A.12}$$

so there cannot be two different potentials that give the same ground state density.
Next we define the energy functional for a given $v(\mathbf{r})$ as

$$E_v[n] = \int v(\mathbf{r})n(\mathbf{r})d\mathbf{r} + F[n], \tag{A.13}$$

where $F[n]$ is a universal functional for the kinetic and interaction energy

$$F[n] = \langle \Psi | T + U | \Psi \rangle . \tag{A.14}$$

For the correct density, $E_v[n]$ gives the ground state energy. We will now show that it is also the minimum value of $E_v[n]$, with the condition

$$N[n] \equiv \int n(\mathbf{r})d\mathbf{r} = N. \tag{A.15}$$

We know that the energy functional of Ψ'

$$\mathscr{E}_v[\Psi'] = \langle \Psi' | V | \Psi' \rangle + \langle \Psi' | T + U | \Psi' \rangle \tag{A.16}$$

has a minimum at the ground state Ψ. Let Ψ' be the ground state associated with a different external potential $v'(\mathbf{r})$. Then with equations A.16 and A.14, we obtain

$$\mathscr{E}_v[\Psi'] = \int v(\mathbf{r})n'(\mathbf{r})d\mathbf{r} + F[n'] > \int v(\mathbf{r})n(\mathbf{r})d\mathbf{r} + F[n] = \mathscr{E}_v[\Psi]. \tag{A.17}$$

Hence, $E_v[n]$ is minimal relative to all other densities associated with other external potential.

A.2 Kohn-Sham Scheme

Following [75] we consider a nondegenerate ground state. We start with an auxiliary system of N non-interacting particles described by the Hamiltonian

$$H_s = T_s + V_s \tag{A.18}$$

According to the Hohenberg and Kohn Theorem, there exists an energy functional

$$E_s[n] = T_s[n] + \int v_s(\mathbf{r}) n(\mathbf{r}) d\mathbf{r}, \tag{A.19}$$

whose minimization gives the ground state density $n_s(\mathbf{r})$. The main argument of Kohn and Sham is that there is single particle potential v_s such that the ground state energy of the interacting system $n(\mathbf{r})$ equals the ground state of the single particle auxiliary system

$$n(\mathbf{r}) = n_s(\mathbf{r}). \tag{A.20}$$

Thus, the equation one has to solve is

$$(\frac{1}{2}\nabla^2 + v_s(\mathbf{r}))\psi_i(\mathbf{r}) = \epsilon_i \psi_i(\mathbf{r}), \tag{A.21}$$

while the density is given by

$$n(\mathbf{r}) = \sum_i^N |\psi_i(\mathbf{r})|^2 . \tag{A.22}$$

Now we need to define v_s. We first define E_{xc} as

$$E_{xc}[n] = F[n] - \frac{1}{2}\int \frac{n(\mathbf{r})n(\mathbf{r}')}{|\mathbf{r}-\mathbf{r}'|} d\mathbf{r} d\mathbf{r}' - T_s[n], \tag{A.23}$$

so that the energy of the interacting system $E_v[n]$ will be given by

$$E_v[n] = T_s[n] + \int v(\mathbf{r}) n(\mathbf{r}) d\mathbf{r} + \frac{1}{2}\int \frac{n(\mathbf{r})n(\mathbf{r}')}{|\mathbf{r}-\mathbf{r}'|} d\mathbf{r} d\mathbf{r}' + E_{xc}[n]. \tag{A.24}$$

According to the Hohenberg Kohn Theorem, the ground state density of the interacting system minimizes $E_v[n]$; thus

$$\left.\frac{\delta E_v[n]}{\delta n}\right|_{n_0} = 0 \tag{A.25}$$

$$\frac{\delta E_v[n]}{\delta n} = \frac{\delta T_s[n]}{\delta n} + v(\mathbf{r}) + \int \frac{n(\mathbf{r}')}{|\mathbf{r} - \mathbf{r}'|} d\mathbf{r}' + \frac{\delta E_{xc}[n]}{\delta n} \tag{A.26}$$

which define the effective potential

$$v_{eff}[n] = v(\mathbf{r}) + \int \frac{n(\mathbf{r}')}{|\mathbf{r} - \mathbf{r}'|} d\mathbf{r}' + \frac{\delta E_{xc}[n]}{\delta n}. \tag{A.27}$$

If we solve self-consistently equation A.21 and A.22 with v_{eff} instead of v_s, we will obtain the exact ground state density of the interacting system. The ground state energy will be given by

$$E_v[n] = \sum_i^N \epsilon_i - \frac{1}{2} \int \frac{n(\mathbf{r}) n(\mathbf{r}')}{|\mathbf{r} - \mathbf{r}'|} d\mathbf{r} d\mathbf{r}' + E_{xc}[n] - \int v_{xc}(\mathbf{r}) n(\mathbf{r}) d\mathbf{r}, \tag{A.28}$$

where

$$v_{xc} = \frac{\delta E_{xc}[n]}{\delta n} \tag{A.29}$$

is the exchange correlation potential.

Appendix B

Detailed Calculation for a Chalker and Coddington Network with Dephasing

Here we present in detail the calculation of the chemical potentials and the currents for a general system following [77]. First we start by writing the scattering equations for each basic unit (Fig B.1) as follows:

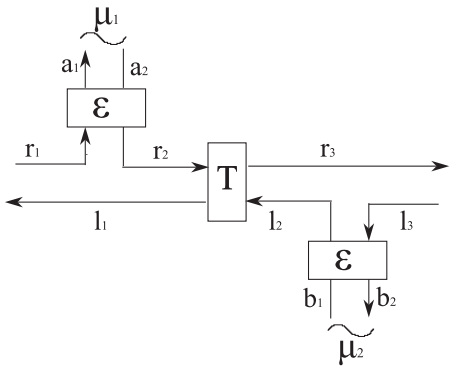

Figure B.1: Basic unit

$$\begin{pmatrix} l_1 \\ r_3 \end{pmatrix} = S_T \begin{pmatrix} r_2 \\ l_2 \end{pmatrix} \tag{B.1}$$

$$\begin{pmatrix} r_2 \\ a_1 \end{pmatrix} = S_\epsilon \begin{pmatrix} r_1 \\ a_2 \end{pmatrix} \tag{B.2}$$

$$\begin{pmatrix} l_2 \\ b_2 \end{pmatrix} = S_\epsilon \begin{pmatrix} l_3 \\ b_1 \end{pmatrix} \tag{B.3}$$

$$S_T = \begin{pmatrix} \sqrt{1-t^2} & it \\ it & -\sqrt{1-t^2} \end{pmatrix} e^{i\phi}, \tag{B.4}$$

where t is the transmission amplitude and ϕ is a random phase.

$$S_\epsilon = \begin{pmatrix} \sqrt{1-\epsilon^2} & i\epsilon \\ i\epsilon & -\sqrt{1-\epsilon^2} \end{pmatrix}, \tag{B.5}$$

where ϵ^2 is the probability of entering the reservoir. Solving of these sets of linear equations gives us the transmission probabilities for all the leads in the network (for the leads that act as a current-conserving reservoir, we set the current at zero). The currents are calculated using the Landauer-Büttiker approach. The system has a source (drain) in the left (right) contact with chemical potential μ_L (μ_R) and N current-conserving reservoirs with chemical potentials μ_i. The current into each reservoir is given by

$$I_i = (1 - R_{ii})\mu_i - \sum_{j \neq i} T_{ij}\mu_j - T_{iL}\mu_L - T_{iR}\mu_R = 0, \tag{B.6}$$

with the use of the unitarity of the s-matrix $T_{iR} = 1 - R_{ii} - \sum_{j \neq i} T_{ij} - T_{iL}$ substituting into Eq.B.6; we thus obtain

$$I_i = (1 - R_{ii})(\mu_i - \mu_R) - \sum_{j \neq i} T_{ij}(\mu_j - \mu_R) - T_{iL}(\mu_L - \mu_R) = 0. \tag{B.7}$$

If we write all the equations in a matrix we obtain:

$$\begin{pmatrix} 1-R_{11} & -T_{12} & \cdots & -T_{1N} \\ -T_{21} & 1-R_{22} & \cdots & -T_{2N} \\ \vdots & & \ddots & \vdots \\ -T_{N1} & \cdots & & 1-R_{NN} \end{pmatrix} \begin{pmatrix} \mu_1-\mu_R \\ \mu_2-\mu_R \\ \vdots \\ \mu_N-\mu_R \end{pmatrix} = \begin{pmatrix} T_{1L} \\ T_{2L} \\ \vdots \\ T_{NL} \end{pmatrix} (\mu_L-\mu_R). \quad \text{(B.8)}$$

The left-hand matrix is conductance matrix $\mathbf{G}$. Multiplying Eq.B.8 by $\mathbf{G}^{-1}$, we obtain

$$\begin{pmatrix} \mu_1-\mu_R \\ \mu_2-\mu_R \\ \vdots \\ \mu_N-\mu_R \end{pmatrix} = G^{-1} \begin{pmatrix} T_{1L} \\ T_{2L} \\ \vdots \\ T_{NL} \end{pmatrix} (\mu_L-\mu_R). \quad \text{(B.9)}$$

Hence the chemical potentials μ_i are

$$\mu_i = \sum_{j=1}^{N} G_{ij}^{-1} T_{jL}(\mu_L-\mu_R)+\mu_R. \quad \text{(B.10)}$$

The current through the sample is

$$I = -(1-R_{RR})\mu_R + T_{RL}\mu_L + \sum_{i=1}^{N} T_{Ri}\mu_i = [T_{RL} + \sum_{i=1}^{N} T_{Ri} \sum_{j=1}^{N} G_{ij}^{-1} T_{jL}](\mu_L-\mu_R) \quad \text{(B.11)}$$

Now we can define $T_{co} \equiv T_{RL}$ and $T_{in} \equiv \sum_{i=1}^{N} T_{Ri} \sum_{j=1}^{N} G_{ij}^{-1} T_{jL}$.

Bibliography

[1] B. J. van Wees, H. van Houten, C. W. J. Beenakker, J. G. Williamson, L. P. Kouwenhoven, D. van der Marel, and C. T. Foxon, "Quantized conductance of point contacts in a two-dimensional electron gas," *Phys. Rev. Lett.*, vol. 60, pp. 848–850, Feb 1988.

[2] K. J. Thomas, J. T. Nicholls, M. Y. Simmons, M. Pepper, D. R. Mace, and D. A. Ritchie, "Possible spin polarization in a one-dimensional electron gas," *Phys. Rev. Lett.*, vol. 77, pp. 135–138, Jul 1996.

[3] S. M. Cronenwett, H. J. Lynch, D. Goldhaber-Gordon, L. P. Kouwenhoven, C. M. Marcus, K. Hirose, N. S. Wingreen, and V. Umansky, "Low-temperature fate of the 0.7 structure in a point contact: A kondo-like correlated state in an open system," *Phys. Rev. Lett.*, vol. 88, p. 226805, May 2002.

[4] D. Goldhaber-Gordon, H. Shtrikman, D. Mahalu, D. Abusch-Magder, U. Meirav, and M. A. Kastner, "Kondo effect in a single-electron transistor," *Nature*, vol. 391, pp. 156–159, 1998.

[5] F. Simmel, R. H. Blick, J. P. Kotthaus, W. Wegscheider, and M. Bichler, "Anomalous kondo effect in a quantum dot at nonzero bias," *Phys. Rev. Lett.*, vol. 83, pp. 804–807, Jul 1999.

[6] D. Goldhaber-Gordon, J. Göres, M. A. Kastner, H. Shtrikman, D. Mahalu, and U. Meirav, "From the kondo regime to the mixed-valence regime in a single-electron transistor," *Phys. Rev. Lett.*, vol. 81, pp. 5225–5228, Dec 1998.

[7] W. G. van der Wiel, S. D. Franceschi, T. Fujisawa, J. M. Elzerman, S. Tarucha, and L. P. Kouwenhoven, "The kondo effect in the unitary limit," *Science*, vol. 289, no. 5487, pp. 2105–2108, 2000.

[8] J. Nygard, D. H. Cobden, and P. E. Lindelof, "Kondo physics in carbon nanotubes," *Nature*, vol. 408, pp. 342–346, 2000.

[9] T. K. Ng and P. A. Lee, "On-site coulomb repulsion and resonant tunneling," *Phys. Rev. Lett.*, vol. 61, pp. 1768–1771, Oct 1988.

[10] Y. Meir, N. S. Wingreen, and P. A. Lee, "Low-temperature transport through a quantum dot: The anderson model out of equilibrium," *Phys. Rev. Lett.*, vol. 70, pp. 2601–2604, Apr 1993.

[11] T. Rejec and Y. Meir, "Magnetic impurity formation in quantum point contacts," *Nature*, vol. 442, pp. 900–903, 2006.

[12] Y. Meir, K. Hirose, and N. S. Wingreen, "Kondo model for the "0.7 anomaly" in transport through a quantum point contact," *Phys. Rev. Lett.*, vol. 89, p. 196802, Oct 2002.

[13] H. Jeong, A. M. Chang, and M. R. Melloch, "The kondo effect in an artificial quantum dot molecule," *Science*, vol. 293, no. 5538, pp. 2221–2223, 2001.

[14] B. A. Jones, C. M. Varma, and J. W. Wilkins, "Low-temperature properties of the two-impurity kondo hamiltonian," *Phys. Rev. Lett.*, vol. 61, pp. 125–128, Jul 1988.

[15] T. Ivanov, "The nonlinear conductance of a double quantum dot in the kondo regime," *EPL (Europhysics Letters)*, vol. 40, no. 2, p. 183, 1997.

[16] T. Aono, M. Eto, and K. Kawamura, "Conductance through quantum dot dimer below the kondo temperature," *Journal of the Physical Society of Japan*, vol. 67, no. 6, pp. 1860–1863, 1998.

[17] A. Georges and Y. Meir, "Electronic correlations in transport through coupled quantum dots," *Phys. Rev. Lett.*, vol. 82, pp. 3508–3511, Apr 1999.

[18] M. J. Iqbal, R. Levy, E. J. Koop, J. B. Dekker, J. P. de Jong, J. H. M. van der Velde, D. Reuter, A. D. Wieck, R. Aguado, Y. Meir, and C. H. van der Wal, "Odd and even kondo effects from emergent localization in quantum point contacts," *Nature*, vol. 501, pp. 79–83, 2013.

[19] B. L. Altshuler, A. G. Aronov, and D. E. Khmelnitsky, "Effects of electron-electron collisions with small energy transfers on quantum localisation," *Journal of Physics C: Solid State Physics*, vol. 15, no. 36, p. 7367, 1982.

[20] A. Stern, Y. Aharonov, and Y. Imry, "Phase uncertainty and loss of interference: A general picture," *Phys. Rev. A*, vol. 41, pp. 3436–3448, Apr 1990.

[21] J. J. Lin and N. Giordano, "Electron scattering times from weak localization studies of au-pd films," *Phys. Rev. B*, vol. 35, pp. 1071–1075, Jan 1987.

[22] D. M. Pooke, N. Paquin, M. Pepper, and A. Gundlach, "Electron-electron scattering in narrow si accumulation layers," *Journal of Physics: Condensed Matter*, vol. 1, no. 20, p. 3289, 1989.

[23] T. Hiramoto, K. Hirakawa, Y. Iye, and T. Ikoma, "Phase coherence length of electron waves in narrow algaas/gaas quantum wires fabricated by focused ion beam implantation," *Applied Physics Letters*, vol. 54, no. 21, pp. 2103–2105, 1989.

[24] H. Taniguchi, T. Nagoya, Y. Takagaki, Y. Yuba, S. Takaoka, K. Gamo, K. Murase, and S. Namba, "Phase coherence length in planar doped thin gaas wires fabricated by

ion beam etching," *Japanese Journal of Applied Physics*, vol. 29, no. Part 1, No. 10, pp. 2321–2325, 1990.

[25] R. Mueller, R. Stasch, and G. Bergmann, "Anomalous t12 law of the dephasing rate in au films down to 20 mk," *Solid State Communications*, vol. 91, no. 3, pp. 255 – 258, 1994.

[26] P. Mohanty, E. M. Q. Jariwala, and R. A. Webb, "Intrinsic decoherence in mesoscopic systems," *Phys. Rev. Lett.*, vol. 78, pp. 3366–3369, Apr 1997.

[27] A. Pouydebasque, A. Pogosov, M. Budantsev, D. Maude, A. Plotnikov, A. Toropov, and J. Portal, "Electron phase coherence length in a lattice of antidots," *Physica B: Condensed Matter*, vol. 298, no. 14, pp. 287 – 290, 2001. ¡ce:title¿International Conference on High Magnetic Fields in Semiconductors¡/ce:title¿.

[28] F. Pierre, A. B. Gougam, A. Anthore, H. Pothier, D. Esteve, and N. O. Birge, "Dephasing of electrons in mesoscopic metal wires," *Phys. Rev. B*, vol. 68, p. 085413, Aug 2003.

[29] C. Bäuerle, F. m. c. Mallet, F. Schopfer, D. Mailly, G. Eska, and L. Saminadayar, "Experimental test of the numerical renormalization-group theory for inelastic scattering from magnetic impurities," *Phys. Rev. Lett.*, vol. 95, p. 266805, Dec 2005.

[30] J. T. Chalker and P. D. Coddington, "Percolation, quantum tunnelling and the integer hall effect," *Journal of Physics C: Solid State Physics*, vol. 21, pp. 2665–2679, 1988.

[31] M. Büttiker, "Four-terminal phase-coherent conductance," *Phys. Rev. Lett.*, vol. 57, pp. 1761–1764, Oct 1986.

[32] D. Shahar, D. Tsui, M. Shayegan, J. Cunningham, E. Shimshoni, and S. Sondhi, "On the nature of the hall insulator," *Solid State Communications*, vol. 102, no. 11, pp. 817 – 821, 1997.

[33] D. Shahar, D. C. Tsui, M. Shayegan, E. Shimshoni, and S. L. Sondhi, "A different view of the quantum hall plateau-to-plateau transitions," *Phys. Rev. Lett.*, vol. 79, pp. 479–482, Jul 1997.

[34] M. Hilke, D. Shahar, S. H. Song, D. C. Tsui, Y. H. Xie, and D. Monroe, "Experimental evidence for a two-dimensional quantized hall insulator," *Nature*, vol. 395, pp. 675–677, 1998.

[35] M. Hilke, D. Shahar, S. H. Song, D. C. Tsui, M. Shayegan, and Y. H. Xie, "The quantized hall insulator," *Ann. Phys. (Leipzig)*, vol. 8, pp. 603–608, (1999).

[36] M. Hilke, D. Shahar, S. H. Song, D. C. Tsui, Y. H. Xie, and M. Shayegan, "Semicircle: An exact relation in the integer and fractional quantum hall effect," *EPL (Europhysics Letters)*, vol. 46, no. 6, p. 775, 1999.

[37] A. Pruisken, D. de Lang, L. Ponomarenko, and A. de Visser, "Universal scaling results for the plateauinsulator transition in the quantum hall regime," *Solid State Communications*, vol. 137, no. 10, pp. 540 – 544, 2006.

[38] A. de Visser, L. A. Ponomarenko, G. Galistu, D. T. N. de Lang, A. M. M. Pruisken, U. Zeitler, and D. Maude, "Quantum critical behaviour of the plateau-insulator transition in the quantum hall regime," *Journal of Physics: Conference Series*, vol. 51, no. 1, p. 379, 2006.

[39] D. T. N. de Lang, L. A. Ponomarenko, A. de Visser, and A. M. M. Pruisken, "Observation of the quantized hall insulator in the quantum critical regime of the two-dimensional electron gas," *Phys. Rev. B*, vol. 75, p. 035313, Jan 2007.

[40] O. Entin-Wohlman, A. G. Aronov, Y. Levinson, and Y. Imry, "Hall resistance in the hopping regime: A "hall insulator"?," *Phys. Rev. Lett.*, vol. 75, pp. 4094–4097, Nov 1995.

[41] L. P. Pryadko and A. Auerbach, "Hall resistivity and dephasing in the quantum hall insulator," *Phys. Rev. Lett.*, vol. 82, pp. 1253–1256, Feb 1999.

[42] U. Zülicke and E. Shimshoni, "Quantum breakdown of the quantized hall insulator," *Phys. Rev. B*, vol. 63, p. 241301, May 2001.

[43] P. Cain and R. A. Römer, "Fluctuating hall resistance defeats the quantized hall insulator," *EPL (Europhysics Letters)*, vol. 66, pp. 104–110, Apr. 2004.

[44] K. Hirose, Y. Meir, and N. S. Wingreen, "Local moment formation in quantum point contacts," *Phys. Rev. Lett.*, vol. 90, p. 026804, Jan 2003.

[45] J. H. Davies, I. A. Larkin, and E. V. Sukhorukov, "Modeling the patterned two-dimensional electron gas: Electrostatics," *Journal of Applied Physics*, vol. 77, no. 9, pp. 4504–4512, 1995.

[46] A. Castro, E. Räsänen, and C. A. Rozzi, "Exact coulomb cutoff technique for supercell calculations in two dimensions," *Phys. Rev. B*, vol. 80, p. 033102, Jul 2009.

[47] P. A. M. Dirac, "Note on exchange phenomena in the thomas atom," *Mathematical Proceedings of the Cambridge Philosophical Society*, vol. 26, pp. 376–385, 1930.

[48] C. Attaccalite, S. Moroni, P. Gori-Giorgi, and G. B. Bachelet, "Correlation energy and spin polarization in the 2d electron gas," *Phys. Rev. Lett.*, vol. 88, p. 256601, Jun 2002.

[49] M. A. Marques, A. Castro, G. F. Bertsch, and A. Rubio, "octopus: a first-principles tool for excited electronion dynamics," *Computer Physics Communications*, vol. 151, no. 1, pp. 60 – 78, 2003.

[50] C. A. Büsser, E. V. Anda, A. L. Lima, M. A. Davidovich, and G. Chiappe, "Transport in coupled quantum dots: Kondo effect versus antiferromagnetic correlation," *Phys. Rev. B*, vol. 62, pp. 9907–9910, Oct 2000.

[51] A. Schmid, "Electron-phonon interaction in an impure metal," *Zeitschrift fr Physik*, vol. 259, pp. 421–436, 1973.

[52] M. Maple, *Magnetism*. Academic, New York, 1973.

[53] P. Nozires, "A fermi-liquid description of the kondo problem at low temperatures," *Journal of Low Temperature Physics*, vol. 17, pp. 31–42, 1974.

[54] Nozières, Ph. and Blandin, A., "Kondo effect in real metals," *J. Phys. France*, vol. 41, no. 3, pp. 193–211, 1980.

[55] G. Zaránd, L. Borda, J. von Delft, and N. Andrei, "Theory of inelastic scattering from magnetic impurities," *Phys. Rev. Lett.*, vol. 93, p. 107204, Sep 2004.

[56] S. Chakravarty and A. Schmid, "Weak localization: The quasiclassical theory of electrons in a random potential," *Physics Reports*, vol. 140, no. 4, pp. 193 – 236, 1986.

[57] R. P. Peters, G. Bergmann, and R. M. Mueller, "Kondo maximum of magnetic scattering," *Phys. Rev. Lett.*, vol. 58, pp. 1964–1967, May 1987.

[58] C. V. Haesendonck, J. Vranken, and Y. Bruynseraede, "Resonant kondo scattering of weakly localized electrons," *Phys. Rev. Lett.*, vol. 58, pp. 1968–1971, May 1987.

[59] J. Vranken, C. Van Haesendonck, and Y. Bruynseraede, "Enhanced magnetic surface scattering of weakly localized electrons," *Phys. Rev. B*, vol. 37, pp. 8502–8505, May 1988.

[60] Y. Niimi, Y. Baines, T. Capron, D. Mailly, F.-Y. Lo, A. D. Wieck, T. Meunier, L. Saminadayar, and C. Bäuerle, "Quantum coherence at low temperatures in mesoscopic systems: Effect of disorder," *Phys. Rev. B*, vol. 81, p. 245306, Jun 2010.

[61] M. A. Ruderman and C. Kittel, "Indirect exchange coupling of nuclear magnetic moments by conduction electrons," *Phys. Rev.*, vol. 96, pp. 99–102, Oct 1954.

[62] T. Kasuya, "A theory of metallic ferro- and antiferromagnetism on zener's model," *Progress of Theoretical Physics*, vol. 16, no. 1, pp. 45–57, 1956.

[63] K. Yosida, "Magnetic properties of cu-mn alloys," *Phys. Rev.*, vol. 106, pp. 893–898, Jun 1957.

[64] K. v. Klitzing, G. Dorda, and M. Pepper, "New method for high-accuracy determination of the fine-structure constant based on quantized hall resistance," *Phys. Rev. Lett.*, vol. 45, pp. 494–497, Aug 1980.

[65] E. Shimshoni, "The quantized hall insulator: a "quantum" signature of a "classical" transport regime?," *Modern Physics Letters B*, vol. 18, pp. 923–943, June 2004.

[66] S. Kivelson, D.-H. Lee, and S.-C. Zhang, "Global phase diagram in the quantum hall effect," *Phys. Rev. B*, vol. 46, pp. 2223–2238, Jul 1992.

[67] A. M. M. Pruisken, "Dilute instanton gas as the precursor to the integral quantum hall effect," *Phys. Rev. B*, vol. 32, pp. 2636–2639, Aug 1985.

[68] E. Shimshoni and A. Auerbach, "Quantized hall insulator: Transverse and longitudinal transport," *Phys. Rev. B*, vol. 55, pp. 9817–9823, Apr 1997.

[69] H. A. Fertig and B. I. Halperin, "Transmission coefficient of an electron through a saddle-point potential in a magnetic field," *Phys. Rev. B*, vol. 36, pp. 7969–7976, Nov 1987.

[70] A. M. Dykhne and I. M. Ruzin, "Theory of the fractional quantum hall effect: The two-phase model," *Phys. Rev. B*, vol. 50, pp. 2369–2379, Jul 1994.

[71] S. V. Kravchenko, G. V. Kravchenko, J. E. Furneaux, V. M. Pudalov, and M. D'Iorio, "Possible metal-insulator transition at $B = 0$ in two dimensions," *Phys. Rev. B*, vol. 50, pp. 8039–8042, Sep 1994.

[72] Y. Hanein, D. Shahar, J. Yoon, C. C. Li, D. C. Tsui, and H. Shtrikman, "Observation of the metal-insulator transition in two-dimensional n -type gaas," *Phys. Rev. B*, vol. 58, pp. R13338–R13340, Nov 1998.

[73] N. Mason and A. Kapitulnik, "True superconductivity in a two-dimensional superconducting-insulating system," *Phys. Rev. B*, vol. 64, p. 060504, Jul 2001.

[74] T.-Y. Huang, C.-T. Liang, G.-H. Kim, C. F. Huang, C.-P. Huang, J.-Y. Lin, H.-S. Goan, and D. A. Ritchie, "From insulator to quantum hall liquid at low magnetic fields," *Phys. Rev. B*, vol. 78, p. 113305, Sep 2008.

[75] W. Kohn and L. J. Sham, "Self-consistent equations including exchange and correlation effects," *Phys. Rev.*, vol. 140, pp. A1133–A1138, Nov 1965.

[76] P. Hohenberg and W. Kohn, "Inhomogeneous electron gas," *Phys. Rev.*, vol. 136, pp. B864–B871, Nov 1964.

[77] J. L. D'Amato and H. M. Pastawski, "Conductance of a disordered linear chain including inelastic scattering events," *Phys. Rev. B*, vol. 41, pp. 7411–7420, Apr 1990.